NTNU

Norwegian University of
Science and Technology

Optical Measurements of Picovibrations on Capacitive Micromachined Ultrasonic Transducers

Mats Marhaug Åldstedt

Master of Science in Electronics
Submission date: June 2010
Supervisor: Astrid Aksnes, IET
Co-supervisor: Erlend Leirset, IET

Problem Description

A new ultrasound element type, the Capacitive Micromachined Ultrasonic Transducer (CMUT) is being developed in connection with the Medical Ultrasound Video Cameras (MUSIC) project. An important part in the development is to perform quality checks of different CMUT prototypes, to make sure the vibration pattern and thereby the acoustic field is the same as modeled.

A heterodyne interferometer has been built for the characterization. The setup can measure the absolute phase and amplitude of surface vibrations with an accuracy of 0.27pm per root Hz. Vibration frequency can range from 10kHz to 1GHz. A network analyzer is also available for additional electrical measurements.

The assignment comprises the characterization of two different CMUT designs optically and electrically. Until now, optical measurements have only been done in air for practical reasons, but the CMUTs designed by MUSIC are meant to operate in a liquid. Since the acoustical impedance is different in air and fluid, the effect of immersing a prototype should also be investigated. The candidate is encouraged to adapt the experimental setup as he or she sees fit.

Assignment given: 15. January 2010
Supervisor: Astrid Aksnes, IET

Abstract

A research group at the Norwegian University of Science and Technology plan to integrate Capacitive Micromachined Ultrasonic Transducers (CMUTs) in a probe which can be used to image human blood vessels from the inside. With CMUT technology still being in its youth, it is important to characterize different CMUT prototypes to learn which design is best suited for the probe. In this thesis, a network analyzer and a heterodyne interferometer are used to characterize two prototypes, both electrically and optically.

The heterodyne interferometer was proven to be extremely sensitive and thus a valuable tool when investigating the behaviour of single CMUT cells. Measurements revealed that the cells within both the CMUT arrays had different resonance frequencies. This effectively broadens the band widths of the prototypes, but reduces their maximum acoustical output power, given that all the cells operate at the same frequency.

It was found probable that the CMUT characteristics were influenced by how charges moved within the prototypes. These charging effects are quite complex and would in practice make it hard to predict where the centre frequency of the CMUT array lies from time to time. The vibration pattern of most the cells at their respective resonance frequencies looked healthy both in air and immersed in a liquid when measuring with the interferometer. Immersed, the resonant frequency range of the CMUT become wider, but the peak was located at a lower frequency than in air.

The next CMUT prototype to be tested in the future does not fit into the experimental setup. A plan to adapt the setup has been presented in this thesis, making it more practical to handle different samples. This design would also make it easier to investigate crosstalk effects between neighboring CMUT elements within the arrays.

Knowledge aquired in this thesis will hopefully help researchers figure out which areas of the CMUT design have the potential to be improved.

Preface

This thesis was written in the fifth and final year of the master's programme in electrical engineering at the Norwegian University of Science and Technology. The work involved being part of a larger research group aiming to create an innovative ultrasound probe. I believe that the ultrasound probe has great potential, but there are still many obstacles to overcome before it can be used as an everyday tool in hospitals. I was happy to contribute to such a large and interesting project. The learning value coming from the experiences over the last semester has been priceless. Reading several books and articles is of course useful, but what I've learned most from is solving problems in cooperation with other people.

I was priveleged to be sent to the Norwegian Electro-optics meeting in Ålesund to present some of my results in April 2010 (the poster is included as a digital appendix outside of this report). People from all corners of the world came to present their research, and there were many fascinating things to learn. I also had the opportunity to present myself to people who might receive a job application from me sometime.

I would like to extend my gratitude to my supervisors Associate Professor Astrid Aksnes and PhD student Erlend Leirset for their guidance and positive attitude. All the other members of the MUSIC group at the university have also been extraordinarily helpful.

Contents

Glossary

AOM Acousto optic modulator.

APD Avalanche photo diode.

BS Beam splitter.

CMUT Capacitive micromachined ultrasonic transducer.

DIP Dual in-line package.

FFC Flexible flat cable.

LIA Lock in amplifier.

MO Microscope objective.

MUSIC Microsystems for Medical Ultrasound Video Cameras.

NTNU Norwegian University of Science and Technology.

PBS Polarizing beam splitter.

QWP Quarter wave plate.

SMT Surface mounted technology.

1 Introduction

1.1 Motivation

Micromachining technology, has among countless other innovative devices opened the door for a new type of ultrasound transducer called the Capacitive Micromachined Ultrasonic Transducer (CMUT). At the Norwegian University of Science and Technology (NTNU), Department of Electronics and Telecommunications there is a research project called Microsystems for Medical Ultrasound Video Cameras (MUSIC). The project aims at designing a probe with CMUTs on the tip in order to image the walls of human coronary arteries by inserting the probe directly into the circulatory system.

Coronary arteries are blood vessels which transfer blood to the heart. For people in the rich parts of the world, an increasing problem is the formation of unstable atherosclerotic plaques within the coronary arteries [1]. Such unstable plaques are in essence pouches of fatty material forming on and in the wall of the arteries. The fat is protected only by a thin membrane which at some point may rupture, possibly causing a coronary infarction. The MUSIC probe will in theory be able to detect vulnerable plaques before they can cause serious or even deadly damage to the heart.

It is believed that a spatial lateral resolution of less than 100μm would be required to image atherosclerotic plaques within an artery. This translates into ultrasonic frequencies in the range $30-50$MHz. Another main challenge in designing the probe is the fact that it must have a maximum diameter of <1mm. Constructing a probe with conventional piezoelectric ultrasound transducers with such demands on size and frequency is difficult and expensive, making the CMUT a good alternative.

A number of CMUT prototypes have been produced for the MUSIC group. Students and staff at the Department of Electronics and Telecommunications at NTNU are now working together to learn about the pros and cons of each prototype. Characterization of the ultrasound transducers is an important step towards ultimately designing the intravascular probe.

In order to measure vibration patterns on the CMUTs' surfaces a heterodyne interferometer has been designed and assembled at NTNU. It can measure picometer scale vibrations at frequencies theoretically up to 1GHz. The interferometer is intended for quality-checks of prototype CMUTs to ensure that the vibration patterns and thereby the acoustic fields are the same as modelled.

1.2   Contribution

This report comprises thorough analyses of the performance of two CMUT pro-
totypes with different designs. The prototypes were first tested electrically in
a network analyzer to locate their respective centre frequencies and to identify
unwanted properties in the frequency responses. Interferometric measurements
allow measurement of single cells in an array of interconnected CMUTs. Such
optical measurements were conducted to get a closer look at the indivudual prop-
erties of the different cells. For example, CMUT cells at the edge of the array
might have different characteristics than the ones at the centre of the array. Such
a phenomenon would not be visible in the electrical measurements because the
network analyzer measures the sum of all interconnected cells rather than single
cells.

Until the end of the last year (2009), interferometric measurements on CMUTs
had only been done in air for practical reasons. Since the CMUTs ultimately will
be used with blood as the surrounding medium, the air-measured characteristics
of the transducers are not the same when they are employed. Recently, the inter-
ferometer setup has been enhanced by the author. The samples are now fastened
in a container so that measurements on immersed samples are possible. Olive
oil has almost the same physical properties as blood plasma and was used as the
surrounding medium for immersed measurements. Both CMUT prototypes were
tested in air, and one of them tested while immersed in oil. Comparison of the
measurement results in air and in oil will be made later in the report.

The newest CMUT prototype from the MUSIC group has quite a different design
with respect to older versions. This new prototype requires another adaptation
of the experimental setup. A CMUT must be connected to a circuit board in
order for it to be excited by voltages in a proper manner. The new CMUT pro-
totype does not physically fit into the old solution for a circuit board. It should
also be easier to move the CMUT with its belonging circuit board from one mea-
surement instrument to another. Therefore, a new and more practical circuit
board capable of holding any CMUT prototype has been designed by the au-
thor and two PhD students at NTNU. The specifications are included in chapter
8. Characterizing the newest prototype is not within the time frame of this thesis.

The results of the measurements and the design of the new circuit board will
be discussed in depth. These discussions will lead to the conclusion in chapter
9.

2 Thesis outline

Chapter 3 will give the appropriate background information needed to understand how the results of this thesis was obtained and their significance. The theory behind the Capacitive Micromachined Ultrasonic Transducer (CMUT) is the most important subject in this chapter, as the report is focused on the characterization of this device. The other subsections in chapter 3 are dedicated to explaining the physics behind the experimental setups. The part concerning heterodyne interferometry will describe qualitatively and mathematically how optical waves can be used to measure vibrations on a surface. A vital part in applying this information in a real heterodyne interferometer is a device called the acousto-optic modulator (AOM). The mechanisms of AOMs are not presumed to be basal knowledge, so some background theory is included. The last subsection in chapter 3 on high-frequency transmission lines explains the nature of the electrical measurements.

Chapter 4 focuses on the experimental setup. Here the heterodyne interferometer will be described both in terms of its optical components, and the electrical components which drive the AOMs and the sample, and process the signal coming from an optical detector.

Chapter 5 is dedicated to determining what size the laser beam has when hitting the sample in the optical setup. The result will give a clue about the spatial resolution of the interferometer.

Chapter 6 involves the first type of CMUT to be characterized. Results of measurements braided with reasons why the particular measurements were conducted will be presented first. There were made both electrical and optical measurements, with a network analyzer and the interferometer, respectively. The results will be thoroughly discussed at the end of this chapter.

Chapter 7 is structured the same way as the previous chapter. Chapter 7 concerns a second prototype CMUT which was not only tested in air, but also immersed in a fluid.

Chapter 8 explains a practical problem with the experimental setup which is introduced by the unorthodox geometric properties of the newest CMUT prototype. A solution to the problem is outlined, which also creates possibilities to measure even more characteristics of the CMUT than at the present time.

Chapter 9 holds the conclusions of this thesis. The discussion from the previous three chapters is taken into account to summarize the most important pieces of new knowledge this thesis has produced.

Appendices A and B are respectively the official data sheets of the AOMs and the optical detector used in the interferometer setup.

Most of the results aquired in chapter 6 were presented by the author at the Norwegian Electro-optics meeting in Ålesund in April 2010. A poster stand was used for the presentation, and the poster is included digitally as an external appendix outside of this report.

3 Theory

This chapter will provide the reader with appropriate background information on several themes. It will be explained in section 3.1 how a Capacitive Micromachined Ultrasonic Transducer (CMUT) works. Sections 3.2 and 3.3 will give an understanding of the physics involved in the interferometric setup. Lastly, section 3.4 includes basic theory on transmission lines and the network analyzer used for electrical measurements of the CMUTs.

3.1 CMUT

The well established piezoelectric ultrasound transducer is on the way to become fully or partially replaced by the capacitive micromachined ultrasonic transducer (CMUT) in ultrasound medical imaging. This prediction is found in numerous papers of late, such as refs. [2], [3], [4]. The most important advantages of the CMUT compared to its piezoelectric counterpart are high frequency bandwidth, smaller size, higher sensitivity and a better electromechanical coupling coefficient (k_t). The fact that the CMUT has a large bandwidth, especially immersed in liquids [2], translates into high spatial and temporal resolution. Piezoelectric transducers are known to have a poor impedance match between the transducer and liquid or tissue medium. CMUTs are made by micromachining techniques which can help improve the impedance matching while keeping the fabrication cost low under batch production [3]. Considering all these advantages, it is clear that the CMUT would be a good alternative when designing a small intravascular ultrasonic probe.

CMUTs were invented in the early 1990s, [5], and design improvements are still being announced from different research groups worldwide.

3.1.1 Principle of operation

A CMUT is an electrostatic transducer used for sound wave excitation and detection. Transduction is obtained by the vibrations of a membrane under the influence of electrostatic forces. Large scale devices which incorporate this effect are well established, such as the condenser microphone. New silicon micromachining technology has now made it possible to create the CMUT, which operates at ultrasonic frequencies [2].

Figure 3.1 shows a cross-section of a standard CMUT cell. Note that due to recent advances, the figure may not be entirely accurate.
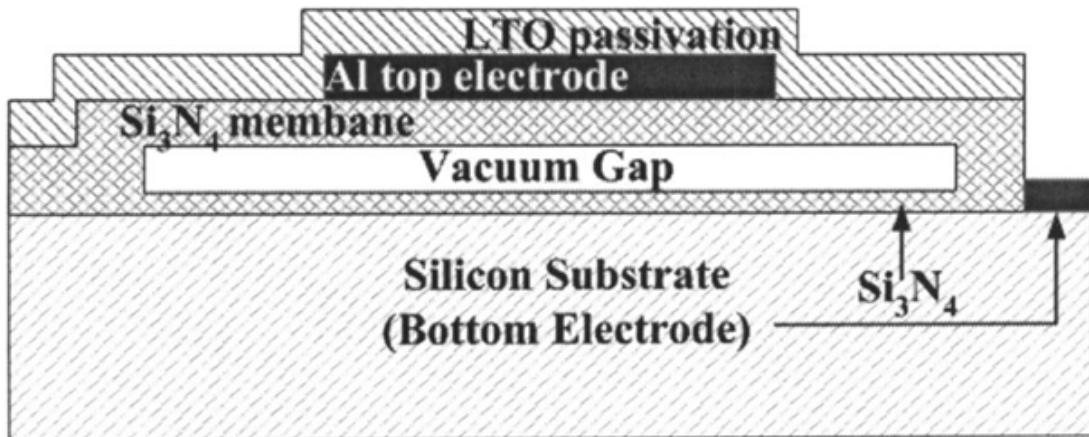
Figure 3.1: Cross-section of a CMUT[1]

As we can see in figure 3.1, the CMUT looks like a parallel plate capacitor made up of the bottom electrode (substrate) and the top electrode on the membrane. CMUTs can be used as both acoustical transmitters and receivers. In transmit mode, the electrostatic attraction forces are used to make the membrane vibrate by applying an AC voltage over the electrodes. The electrostatic forces originating from this AC voltage is however unipolar, so the membrane vibrates at a frequency which is twice that of the applied AC excitation. A DC bias voltage, stronger than the amplitude of the AC voltage, must therefore be applied for the CMUT to work properly [2]. Ultrasonic waves will originate at the membrane when it starts moving, and the waves will be spread through the surrounding medium.

It is now established that the voltage over the electrodes introduces an electrostatic force which pulls the membrane towards the substrate. A mechanical restoring force due to the stiffness of the membrane also acts on it in the other direction, like a spring would. This restoring force keeps the membrane stretched towards the substrate, but the membrane will not accelerate if the voltage is a steady bias. The deflection distance will be longer as the voltage is increased. However if the bias exceeds a certain value, the electrostatic forces will become too strong for the mechanical restoring force, and the membrane collapses on to the substrate. This bias level is called the collapse voltage. Research has submitted that the device has best efficiency close to, but not above the collapse voltage [2].

Figure 3.2 shows a circuit model for how the CMUT works in transmit mode.

---

[1]Figure is from ref. [2]
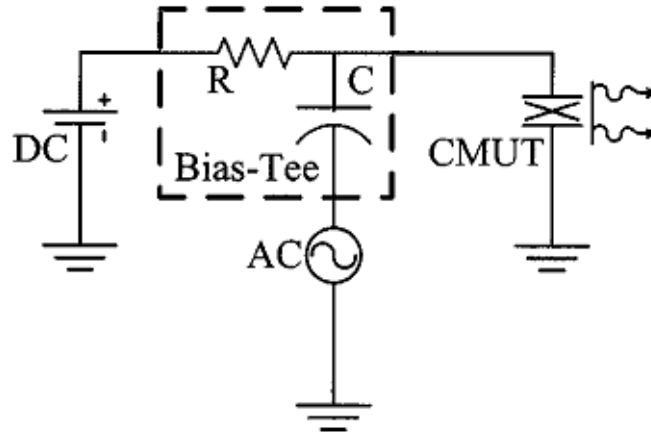
Figure 3.2: Circuit model for a CMUT in transmit mode[1]

Let us consider the receive mode. If there is an incident acoustic wave, the membrane will start vibrating. This vibration is analogous to change in capacitance between the electrodes, and is detected if we have applied a DC bias voltage. Under influence of the bias voltage and capacitance change, a current will be induced in the external circuit [2] shown in figure 3.3. This signal current is amplified and coupled to an output terminal for further processing.
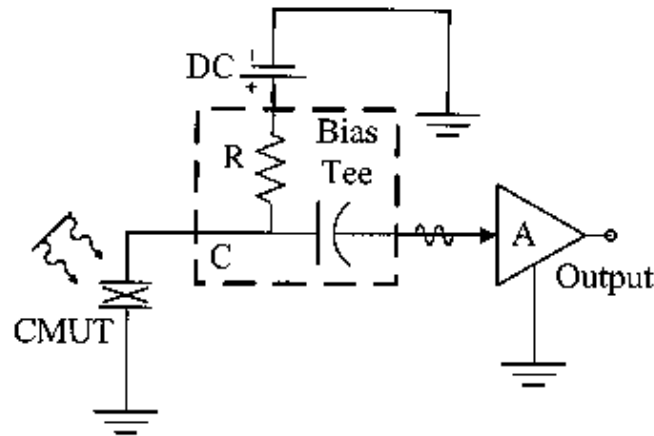
Figure 3.3: Circuit model for a CMUT in receive mode[1]

CMUTs have both symmetric and anti-symmetric resonant modes of vibration. It is the first and fundamental mode which is used in the transducer's applications, so the transducer is generally operated at a certain frequency. Where these resonance frequencies are located, depends on the CMUT geometrical dimensions, materials and bias voltage [6]. Ref. [7] has submitted that the vibration amplitude

---

[1]Figure is from ref. [2]

of the CMUT is proportional to the applied AC voltage. The AC level does not have an effect on the location of the resonance frequency, though. The bandwidth of the CMUT varies with the surrounding medium, but the general rule is that the bandwidth is wider in immersion than in air [2].

3.1.2 Fabrication and prototypes

In order to obtain the wanted acoustic power, several CMUT cells are created next to each other as an interconnected array. Several authors have described ways of fabricating CMUTs, such as [8], [9] and [10]. There are however two general methods outlined.

The first, and still widely used method, is called the sacrificial release process, which is a surface micromachining process. Surface micromachining means that the transducers are made by use of thin-film depositions, thin-film etching and photolithography on top of a wafer substrate, rather than etching structures into the substrate itself. The substrate acts as a bottom electrode, and is heavily doped in order to achieve high conductivity. On top of this bottom electrode, there is a layer of silicon nitride and a vacuum gap inside it. The cavity is created by depositing a sacrificial layer on the first silicon nitride layer. This sacrificial layer is wet etched away after the membrane layer has been deposited, and then the aluminum connection pads are put in place. One is connected to the membrane surface and the other to the substrate. The electrodes are then covered with a low temperature oxide (LTO) passivation layer and epoxy in order to contain the electricity in conductive fluids and avoid corrosion [2].

The second method is known as the wafer bonding technique. Here two silicon-on-insulator wafers are used to create the CMUTs. On the first wafer, the cavity structures are selectively etched into the silicon. The second wafer is put in a deposition chamber. Here a thin layer of silicon nitride is grown on top of the wafer which will become the membrane. The two wafers are then bonded together in a vacuum environment after a heat treatment. By removing the silicon of the second wafer, what remains is a series of cavities with membranes stretched above. Lastly, the aluminum top electrodes are deposited on top of the membranes [8]. Wafer bonding is considered a more reliable way of making CMUTs under batch production [2].

The two varieties of CMUT prototypes measured in this thesis are fabricated using the wafer bonding technique. The prototypes were produced at SINTEF's micro- and nanotechnology laboratory in Oslo. Ref. [8] has a detailed description of the fabrication process.

3.2 Heterodyne Interferometry

Interferometry is according to ref. [11] related to the physical phenomena which result from the superposition of electromagnetic waves. The radiation typically emerges from the same source and travels along different paths to a point where it is detected. Interferometry is in other words the technique of diagnosing the properties of two or more electromagnetic waves by observing the way they interfere with each other. The goal is to extract information about where these waves have been. If they are propagating at different frequencies the interferometer is heterodyne, as the name suggests. A photo detector receiving the waves will observe the interference as beats of light if the waves have different frequencies [12].

The first requirement for stationary optical interference is a coherent light source [13]. Coherence means that the waves emitting from the source have the same phase. The laser is the superior alternative when it comes to choosing the optical source for interferometry; its light is highly coherent, intense and collimated [12].

The solutions of Maxwell's equations [14] support the previously mentioned superposition principle. The total field in some arbitrary position $\vec{r}$ resulting from two fields overlapping in space and time can thus be expressed as the vectorial sum of the two original fields. This is written in mathematical terms in equation 3.1:

$$\vec{E}_{tot}(\vec{r},\nu) = \vec{E}_1(\vec{r},\nu) + \vec{E}_2(\vec{r},\nu) \tag{3.1}$$

$\vec{E}_{tot}$ Total electric field
$\vec{r}$ Position vector
ν Optical frequency
$\vec{E}_1$ Electric field from first source or virtual source
$\vec{E}_2$ Electric field from second source or virtual source

Current technology can not detect the complex fields for optical frequencies, only time averaged intensity. The total intensity can according to ref. [12] be expressed as equation 3.2. It is assumed that the fields are monochromatic and are travelling in the same direction.

$$I = |A_1 + A_2|^2 \qquad (3.2)$$

|	
I	Total intensity
A_1	Complex amplitude of first field, $A_1 = a_1 \mathrm{e}^{-j\phi_1}$
A_2	Complex amplitude of second field, $A_2 = a_2 \mathrm{e}^{-j\phi_2}$
ϕ_1	Phase of the field from first source or virtual source
ϕ_2	Phase of the field from second source or virtual source

If we expand this expression using rules of complex numbers and trigonometric functions [15] we get equation 3.3:

$$
\begin{aligned}
I &= A_1^2 + A_2^2 + A_1 A_2^* + A_1^* A_2 \\
  &= I_1 + I_2 + 2\sqrt{I_1 I_2}\cos(\phi_2 - \phi_1)
\end{aligned}
\qquad (3.3)
$$

I_1	Intensity of the first source or virtual source
I_2	Intensity of the second source or virtual source

I_1 here is the intensity of the first field and I_2 is the intensity of the second field. The third term is the interference term, and the general concept of interferometry is to find a value for the phase difference in the interference term by just measuring the intensity. That way it is possible to extract information about physical properties that affect this phase difference.

One way of using the phase difference is to send one of the waves through a sample in order to measure the refractive index of the material. Figure 3.4 shows a setup that illustrates this simple interferometer setup. It is called a Mach-Zehnder interferometer [16].
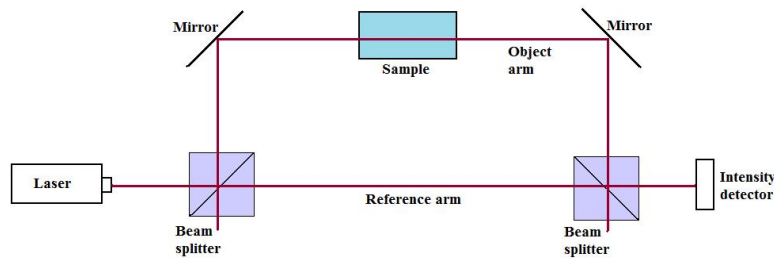

Figure 3.4: Mach-Zehnder interferometer

The laser emits a light beam which is split in the first beam splitter. This causes some of the light to get reflected through the sample, while the remaining portion of the incoming intensity penetrates the beam splitter and continues along the same path. The unaffected beam is called the reference beam and the reflected beam is known as the object beam. As figure 3.4 suggests, the object beam is led by mirrors through the sample and then into another beam splitter. If the beam splitters are properly aligned, a portion of each of the beams will enter the detector with the conditions of interference intact.

The refractive index of the sample will determine the optical path length of the object arm and thus the phase difference between the beams. As already presented, this phase difference affects the interference part of the intensity equation. By looking at the intensity at the detector it is therefore possible to measure the physical properties which modulate the refractive index of the sample.

Mathematically speaking, the sample introduces a shift in the original phase of the object arm in equation 3.3 by $\frac{2\pi}{\lambda_0}(n_s - n_a)L$ where λ_0 is the vacuum wavelength of the laser, n_s and n_a are the refractive indices of the sample and the surrounding medium, respectively, and L is the length through the sample. If equation 3.3 is the intensity at the detector in figure 3.4 without the sample in the object arm, equation 3.4 would be correct when the sample is in place.

$$I_d = I_{ref} + I_{obj} + 2\sqrt{I_{ref}I_{obj}}\cos(\phi_{ref} - (\phi_{obj} + \frac{2\pi}{\lambda_0}(n_s - n_a)L)) \qquad (3.4)$$

I_d	Total intensity at the detector
I_{ref}	Intensity of the reference beam
I_{obj}	Intensity of the object beam
ϕ_{ref}	Phase of the reference beam
ϕ_{obj}	Phase of the object beam
λ_0	Vacuum wavelength of laser
n_a	Refractive index of surrounding medium
n_s	Refractive index of sample
L	Length of sample
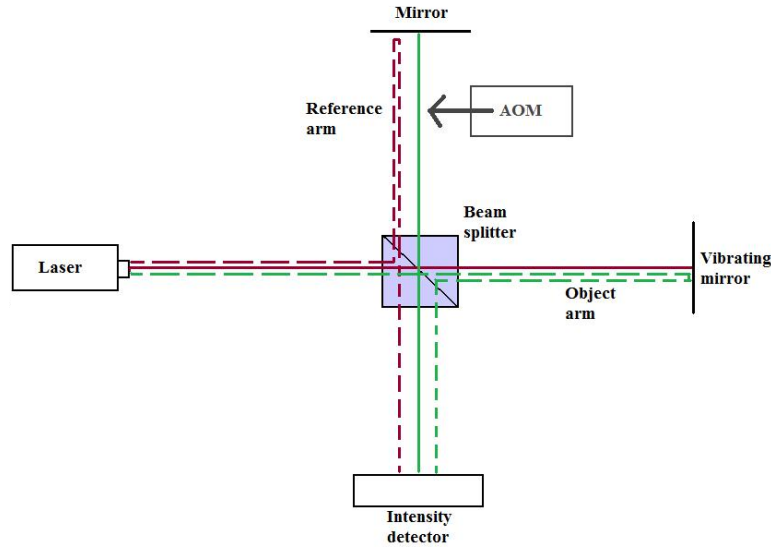
Figure 3.5: Michelson interferometer

Figure 3.5 shows another basic setup, it is a typical Michelson interferometer [14]. One single beam splitter is used both to split and recombine the beam in this case. The basic idea behind the setup is to be able to measure any vibrations of the mirror on the right in figure 3.5, using the modulation of the phase difference of the interference term in equation 3.3. However, if the mirror's vibrations are small, the response read out at the detector might be buried in noise.

An acousto-optic modulator (AOM) can be inserted into the reference arm in order to change the optical frequency in this arm slightly. Due to the frequency difference between the two interferometric arms, the cosine term in equation 3.3 will get time dependence, and the photo detector will observe beats of light [12]. Equation 3.5 describes the detected intensity, given that the right mirror is stationary. More on AOMs in section 3.3.

$$I_d = I_{ref} + I_{obj} + 2\sqrt{I_{ref}I_{obj}}\cos(2\pi f_m t + \phi_{ref} - \phi_{obj}) \qquad (3.5)$$

f_m Frequency shift caused by AOM

The mirror on the right in figure 3.5 starts vibrating slightly. Equation 3.6 shows the sinusoidal displacement of the mirror if it was in equilibrium position to begin with [16].

12

$$\Delta r = a \sin(2\pi f_a t + \phi_a) \tag{3.6}$$

Δr Instantaneous displacement of the mirror
a Absolute amplitude of the mirror vibrations
f_a Frequency of the mirror vibrations
ϕ_a Phase of the mirror vibrations

The vibrating mirror causes the optical path length of the object beam to become modulated by twice the displacement in equation 3.6. This does in turn introduce a sinusoidal phase modulation of the intensity. Equation 3.7 shows the intensity which is coming into the detector from the combined object and reference arms [16]. It is assumed that the beams coming into the detector are collinear and have the same polarization states. Also, the optical frequencies have been time averaged while the other frequency variables are not. This is an acceptable approximation because the optical frequencies are assumed to be much higher than f_a and f_m. The optical frequencies cannot, as noted earlier, be detected by present technology.

Figure 3.6 illustrates how the detected intensity with and without mirror vibration might look like, though exaggerated.

$$I_d = I_{ref} + I_{obj} + 2\sqrt{I_{ref}I_{obj}}\cos(2\pi f_m t - \frac{4\pi a}{\lambda}\sin(2\pi f_a t + \phi_a) + \phi_{ref} - \phi_{obj}) \tag{3.7}$$

λ Laser wavelength in the medium surrounding the interferometer
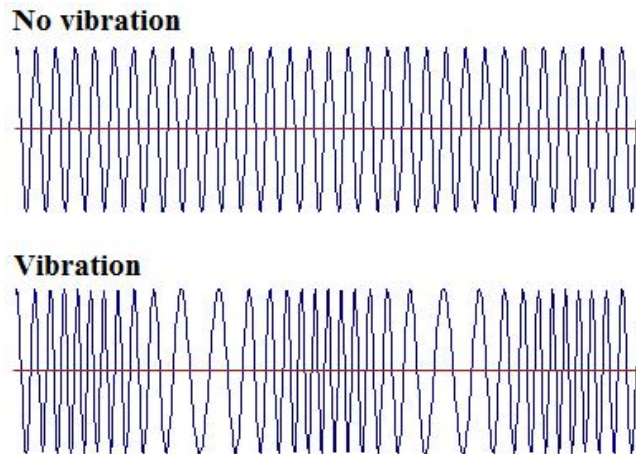
Figure 3.6: Detector signal with and without mirror vibrations

There is more than one approach to demodulating the signal [16] and retrieving the vibration amplitude, but the one to be presented here is going to be used for

the rest of the report. The time dependent part of equation 3.7 is rewritten in equation 3.8, using the real part of a complex exponential function [16]. Applying a first order Taylor series on the expression will result in equation 3.9. This is a good approximation since $\frac{4\pi a}{\lambda}$ is assumed to be much smaller than unity [16].

$$I_{d,ac} = 2\sqrt{I_{ref}I_{obj}} \cdot \Re\left[e^{j(2\pi f_m t - \frac{4\pi a}{\lambda}\sin(2\pi f_a t + \phi_a) + \phi_{ref} - \phi_{obj})}\right] \tag{3.8}$$

$$= 2\sqrt{I_{ref}I_{obj}} \cdot \Re\left[e^{j(2\pi f_m t + \phi_{ref} - \phi_{obj})} \cdot e^{-j\frac{4\pi a}{\lambda}\sin(2\pi f_a t + \phi_a)}\right]$$

$$\approx 2\sqrt{I_{ref}I_{obj}} \cdot \Re\left[e^{j(2\pi f_m t + \phi_{ref} - \phi_{obj})}\left(1 - j\frac{4\pi a}{\lambda}\sin(2\pi f_a t + \phi_a)\right)\right] \tag{3.9}$$

$I_{d,ac}$ Time dependent part of intensity at detector

Looking closely at equation 3.9, one can see that there are two terms, and that the real part of each of them can be found. Doing that, we end up with equation 3.10. Credit for calculating this goes to ref. [16].

$$\begin{aligned} I_{d,ac} &= 2\sqrt{I_{ref}I_{obj}} \cdot \cos(2\pi f_m t + \phi_{ref} - \phi_{obj}) \\ &+ 2\sqrt{I_{ref}I_{obj}} \cdot \frac{4\pi a}{\lambda}\sin(2\pi f_a t + \phi_a) \cdot \sin(2\pi f_m t + \phi_{ref} - \phi_{obj}) \end{aligned} \tag{3.10}$$

Applying trigonometric product formulas [15] in the second term of equation 3.10, the result is three purely harmonic terms for the detected time dependent intensity [7], equation 3.11.

$$\begin{aligned} I_{d,ac} &= 2\sqrt{I_{ref}I_{obj}} \cdot \cos(2\pi f_m t + \phi_{ref} - \phi_{obj}) \\ &+ 2\sqrt{I_{ref}I_{obj}} \cdot \frac{2\pi a}{\lambda}\cos(2\pi(f_a - f_m)t + \phi_a - \phi_{ref} + \phi_{obj}) \\ &+ 2\sqrt{I_{ref}I_{obj}} \cdot \frac{2\pi a}{\lambda}\cos(2\pi(f_a + f_m)t + \phi_a + \phi_{ref} - \phi_{obj}) \end{aligned} \tag{3.11}$$

If I_d is measured for a period of time, it is possible to Fourier transform these terms one by one into the frequency domain. As to be evident soon, only the two first terms in the frequency domain are needed to extract the absolute amplitude and phase of the vibrations. The complex amplitudes of the f_m and $f_a - f_m$ frequency components are expressed in equations 3.12 and 3.13, respectively [7].

$$R_i = 2\sqrt{I_{ref}I_{obj}} \cdot \frac{2\pi a}{\lambda} \mathrm{e}^{j(\phi_a - \phi_{ref} + \phi_{obj})} \tag{3.12}$$

$$R_n = 2\sqrt{I_{ref}I_{obj}} \cdot \mathrm{e}^{j(\phi_{ref} - \phi_{obj})} \tag{3.13}$$

R_i	Complex amplitude of detected intensity at frequency $f_a - f_m$
R_n	Complex amplitude of detected intensity at frequency f_m

Now it is possible to solve the vibrations' amplitude and phase. The absolute vibration amplitude a and phase ϕ_a can evidently be calculated by measuring the amplitudes of R_i and R_n simultaneously and using equation 3.14, [7].

$$a \cdot \mathrm{e}^{j\phi_a} = \frac{\lambda}{2\pi} \cdot \frac{R_i}{R_n^*} \tag{3.14}$$

If equation 3.9 had been approximated with a second order Taylor series, the vibration amplitude would have been expressed by equation 3.15, though the phase would have been the same [16].

$$a = \frac{\lambda}{4\pi} \cdot \frac{\sqrt{1 + 4 \cdot |R_i/R_n|^2} - 1}{|R_i/R_n|} \tag{3.15}$$

3.3 Acousto-optics

Acousto-optics is a relatively new science, dating from 1922 when Léon Brillouin predicted that light might be scattered by sound waves. This area of science was purely academic until the first lasers were built in the 1960s when the acousto-optic effect became useful [17]. Acousto-optic devices are today an important part of many academic and commercial systems. These include optical modulators, switches, deflectors, filters, isolators, frequency shifters and spectrum analyzers.

3.3.1 The acousto-optic effect

Acoustic waves, or sound waves, are dynamic strains which involve molecular vibrations. These vibrations travel at a velocity that is characteristic for the certain medium in which they are propagating. As the molecular structure in a volume of the medium is contracted, the density increases, thus making the refractive index larger. When the volume is stretched, the refractive index becomes smaller. That means that acoustic waves have the ability to interact with optical waves.

The acoustical frequencies are assumed to be much lower than the optical frequencies. It is therefore adequate to view the medium with the acoustic waves as quasi time stationary, but with a spatial dependent and periodic refractive index [14].

One of the simplest forms of acousto-optic interaction is the partial reflection of optical plane waves on the stratified parallel planes representing the refractive index variations caused by an acoustical plane wave. In ref. [14] we find the expression for the amplitude reflectance of the optical waves on a front of refractive index variation. It is stated in equation 3.16. The reflectance coefficient r_0 is related to the length of the interaction medium, a material parameter and the intensity of the sound. The terms r_+ and r_- are called the upshifted and downshifted reflections, respectively. The reason for this will be explained shortly.

$$r_{\pm} = \pm j r_0 \text{sinc}[(2k \sin\theta \mp q)\frac{L}{2\pi}]e^{\pm j\Omega t} \tag{3.16}$$

$r_{\pm}$	Up- and downshifted reflection coefficients
r_0	Arbitrary reflection coefficient
k	Optical wave number
θ	Angle of optical wave's incidence
q	Acoustical wave number
L	Length of interaction medium
Ω	Angular frequency of acoustic wave

Let us for simplicity's sake only look at the upshifted reflection first. If the optical waves have an angle of incidence θ_B so that the incremental reflections from the planes separated by an acoustic wavelength Λ have a phase shift of 2π, they will interfere completely constructively. The socalled Bragg condition is satisfied[14], and the sinc function of equation 3.16 reaches its maximum of unity in the case of upshifted reflection. The Bragg condition is stated in equation 3.17 and figure 3.7 illustrates the Bragg reflections.

$$\sin\theta_B = \frac{\lambda}{2\Lambda} \tag{3.17}$$

θ_B	Bragg angle of incidence
λ	Wavelength of optical wave
Λ	Wavelength of acoustic wave

It is also possible to express the Bragg condition as a relation between the wave vectors of the sound wave and the optical waves [14]. Let us say that $\vec{q} = (q, 0, 0)$, $\vec{k} = (-k\sin\theta, 0, k\cos\theta)$ and $\vec{k_r} = (k\sin\theta, 0, k\cos\theta)$ are the components of the wave vectors of the sound wave, the incident light wave, and the reflected light wave, respectively. Then the Bragg condition stated in equation 3.17 is equivalent to the vector relation in equation 3.18. The vector relation is illustrated in figure 3.8 , when assuming that the two wave vectors $\vec{k}$ and $\vec{k_r}$ have approximately the same length. This assumption is acceptable to make because the component of $\vec{k_r}$ perpendicular to $\vec{q}$ is unaltered and the frequency difference is relatively small compared to the optical frequencies of the waves.

$$\vec{k_r} = \vec{k} + \vec{q} \tag{3.18}$$

$\vec{k_r}$	Wave vector of reflected optical wave
$\vec{k}$	Wave vector of incident optical wave
$\vec{q}$	Wave vector of acoustic wave

Reviewing equation 3.16 it is clear that the complex amplitude reflectance r_+ is proportional to $e^{j\Omega t}$. The angular frequency of the incident light is ω , i.e.
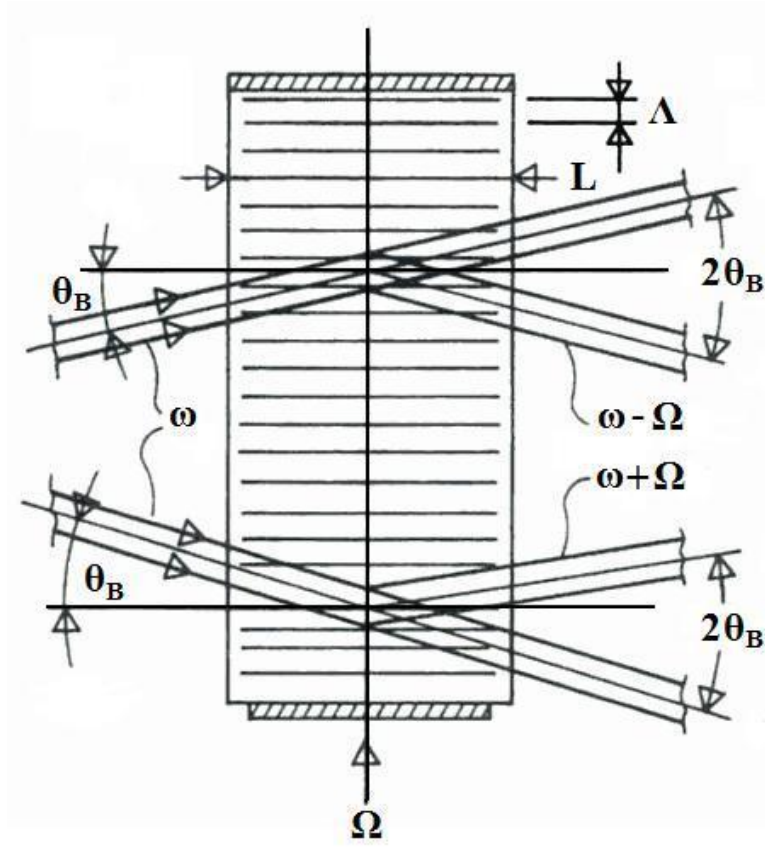
Figure 3.7: Bragg reflections[2]

the amplitude E of the light is proportional to $e^{j\omega t}$. Taking the product of the reflectance coefficient r_+ and E, it is easy to obtain the expression in equation 3.19 for the angular frequency of the reflected light.

$$E_r = r_+ E \propto e^{j(\omega + \Omega)t}$$

$$\omega_r = \omega + \Omega \tag{3.19}$$

E_r	Amplitude of reflected optical wave
E	Amplitude of incident optical wave
ω	Angular frequency of incident optical wave
ω_r	Angular frequency of reflected optical wave

The process of reflection is in other words accompanied by a shift in frequency equal to that of the acoustic wave. Using the same train of thought with an angle of incidence $-\theta_B$ instead of θ_B, the angular frequency of the light would be shifted downwards, i.e. $\omega_r = \omega - \Omega$.

---

[2]Figure is edited from ref. [17]
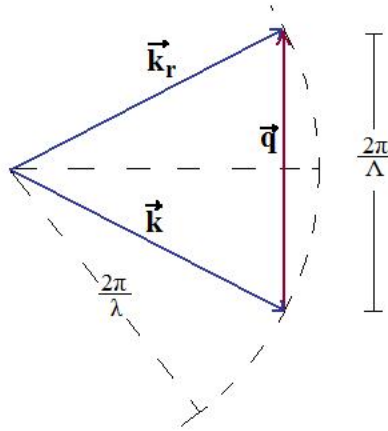
Figure 3.8: Bragg condition with vectors

If this is a bit difficult to grasp, try thinking of it as a Doppler shift, analogous to the frequency shift that happens when a sound is reflected from a moving surface.

3.3.2 Acousto-optic modulators

An acousto-optic modulator (AOM) is a device which puts this theory into practice. Basically it consists of a crystal or a piece of glass through which the light is propagating. In one end there is a transducer which produces the sound waves that go through the crystal in the order of 100 MHz. In the other end there are two possibilities. There might be installed an acoustical absorber in order to remove any reflections. Such devices have a good modulation bandwidth of several MHz. The other possibility is to have a reflector at the end. This reflector will make it possible to induce resonance in the crystal, and the resonant enhancement can greatly increase the modulation strength (or decrease the required acoustic power), but reduces the modulation bandwidth [18].

The acoustic beam acts in practice as a diffraction grating since the divergence of the optical beam is much larger than the acoustical wavelength Λ. Several orders of the diffraction maxima may be visible at the same time. The optical frequency of the higher order maxima will not be the same as of the zeroth or first order. This can be explained by reviewing the vector relation in equation 3.19 and looking at figure 3.9. The wave vector of the mth order maximum is a sum of the incoming wave vector $\vec{k}$ and $m\vec{q}$. The term $m\vec{q}$ comes from the variant angle of deflection. Equations 3.18 and 3.19 can now be generalized to 3.20 and 3.21.
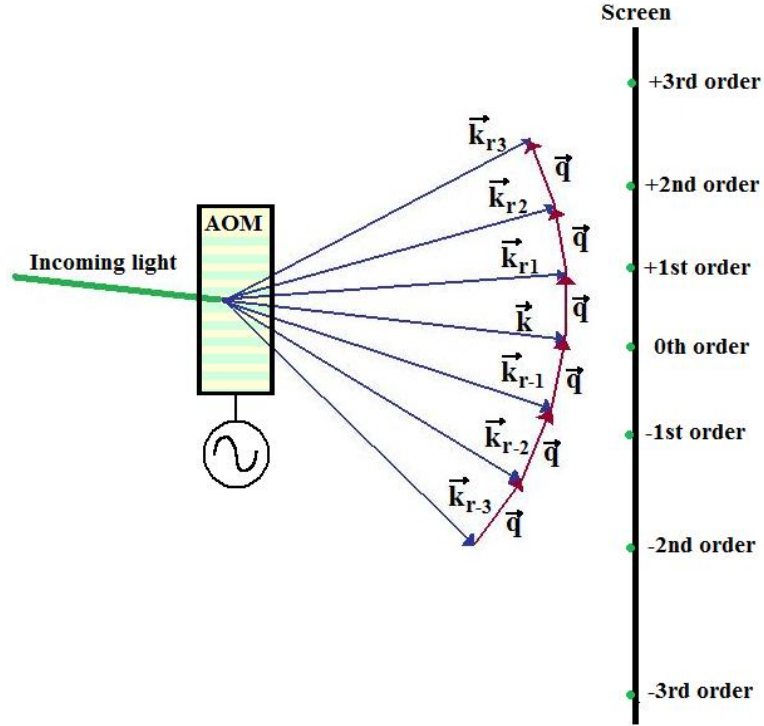
Figure 3.9: Diffractive orders

$$\vec{k_r} = \vec{k} + m\vec{q} \tag{3.20}$$

$$\omega_r = \omega + m\Omega \tag{3.21}$$

$$m = \ldots -2, -1, 0, 1, 2 \ldots$$

When applying AOMs to useful systems, it is common to either use the positive or negative 1st order maxima because these are most intense. The angle of the incoming optical beam should be aligned so that the wanted order gets the highest possible output intensity. If the device is aligned correctly and has high acoustic power, more than 50 % of the incoming laser power can be diffracted to the first order [18].

3.4 High-frequency transmission lines

3.4.1 Transmission lines

In many electric circuits, the voltage on a wire connecting two components can be assumed to be the same in every place along the wire at a given time. However, when operating at high signal frequencies the picture becomes slightly more complicated. The general rule is that the wire must be viewed as a transmission line when the signal contains frequency components with wavelengths comparable to or less than the physical length of the wire [19]. On a transmission line, the voltages and currents can change in magnitude and phase over the length of the line. That is, the voltages and currents have the same properties as waves.
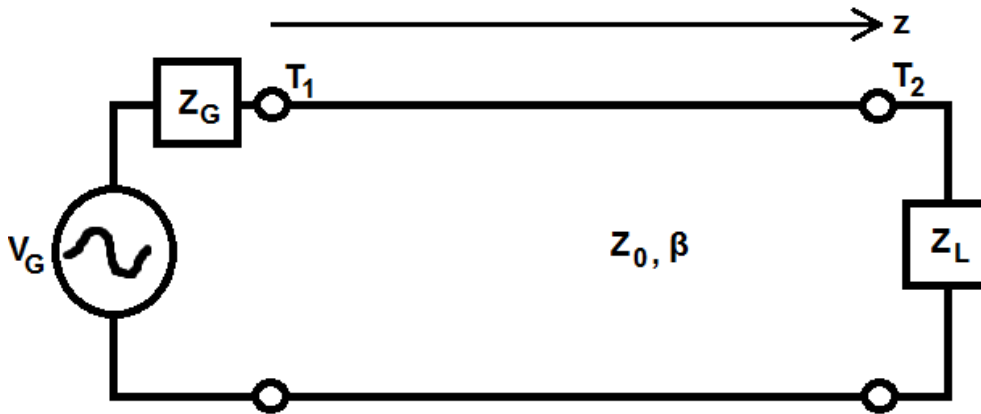
Figure 3.10: Transmission line circuit

Figure 3.10 shows a simple circuit which may help illustrate the effects of a transmission line when operating at a high frequency. For simplicity, it is assumed that this transmission line is lossless. On the left side of the circuit, there is an AC generator applying voltage over the built-in generator impedance Z_G and the load with an impedance Z_L. As a side-note, $Z_G = 50\Omega$ for most commercial generators. On the transmission line between terminals T_1 and T_2 the input voltage travels like a wave, as we established in the previous paragraph. In mathematical terms, the complex voltage wave incident from T_1 at a point z along the wire is expressed as $V_0^+ e^{-j\beta z}$. V_0^+ is the peak amplitude of the signal at T_1 and β is the complex, frequency dependent propagation constant. The ratio of voltage to current on the transmission line is defined as the characteristic impedance Z_0. This ratio is the same all over the transmission line until the wave reaches the load Z_L at terminal T_2. At the load, the ratio of voltage to current must be equal to Z_L. To satisfy this condition, a portion of the wave must be reflected back if $Z_0 \neq Z_L$ [19]. The total voltage on the transmission line can thus be expressed as the sum of incident and reflected voltage waves, see equation 3.22. The first term represents the incident wave and the second denotes the reflected wave, respectively.

$$V(z) = V_0^+ \mathrm{e}^{-j\beta z} + V_0^- \mathrm{e}^{j\beta z} \qquad (3.22)$$

$V(z)$	Total voltage on the line in position z
V_0^+	Amplitude of incident wave
V_0^-	Amplitude of reflected wave
β	Propagation constant

3.4.2   Scattering parameters

Figure 3.10 showed a simple network with only one input/output terminal, referred to as a port. There may however be many ports in a complicated network, each with their own incident and reflected voltage wave. To achieve a complete description of a network as seen from all its ports, the scattering matrix, or S-matrix, is widely used. The S-parameters in the matrix relates the incident voltage waves on the ports to those reflected from the ports [19]. According to ref. [19], the S-matrix representation is especially useful when operating at frequencies high enough to make it difficult to measure total voltages and currents, but still easy to measure incident and reflected voltage waves. Once the S-matrix is calculated or measured, it can be converted to other matrix representations, if needed.

The scattering matrix of a network with N ports is defined as in equation 3.23, and a particular element in the S-matrix can be found using equation 3.24 [19].

$$
\begin{bmatrix} V_1^- \\ V_2^- \\ . \\ . \\ . \\ V_N^- \end{bmatrix}
=
\begin{bmatrix}
S_{11} & S_{12} & . & . & . & S_{1N} \\
S_{21} & . & & . & . & . \\
. & . & & . & . & . \\
. & . & & . & . & . \\
. & . & & . & . & . \\
S_{N1} & . & & . & . & S_{NN}
\end{bmatrix}
\begin{bmatrix} V_1^+ \\ V_2^+ \\ . \\ . \\ . \\ V_N^+ \end{bmatrix}
\qquad (3.23)
$$

$$S_{mn} = \frac{V_m^-}{V_n^+} \Bigg|_{V_p^+ = 0 \,\text{for}\, p \neq n} \qquad (3.24)$$

V_m^-	Amplitude of reflected wave from port m
S_{mn}	Scattering parameter
V_n^+	Amplitude of incident wave at port n

Equation 3.24 explains mathematically that S_{mn} is found by driving port n with an incident voltage wave V_n^+ and measuring the reflected wave with an amplitude V_m^- at port m. There should be no incident waves at any other port than n, and these other ports should be terminated by a matched load to prevent reflections from the connections. Such reflections would amount to incident waves [19].

3.4.3 Network analyzers

The network analyzer is a good tool for determining how a network responds to signals of different frequencies [20]. Most network analyzers have their own signal generator which is connected to the network to be measured. The sample is viewed as a "'black box'", i.e. the analyzer is only meant to probe at the ports of the circuitry. While the generator applies voltage on one of the ports, the network analyzer can listen to one or more ports to register the reflected waves. The user can save the results in a data file, for example as an S-parameter representation [20].

Calibration is a major issue when working with network analyzers. If the sample is measured without calibrating first, systematic errors will appear in the results [20]. These errors come from the fact that the wire connecting the analyzer to the network also becomes a part of the sample in the eyes of the analyzer, effectively adding more length to the transmission line. Modern network analyzers can be calibrated in such a way that the measurements are done at the end of the connection wire. This calibration is performed by terminating the wire coming from the analyzer with three known loads: open, short and 50Ω. The network analyzer then calibrates itself so that the measured results become equal to the expected results. It must be noted that even small temperature changes in the wire might require a new calibration due to the changing wire length [20].

The networks measured in this thesis were CMUT samples, which are 1-port networks with a capacitive load. Measuring the input reflection coefficient S_{11} in a frequency range gives the opportunity of determining the resonance frequency of the CMUTs. In the non-resonant frequency range, S_{11} would probably look like a smooth sinusoidal curve. This is due to the fact that it is hard to calibrate exactly at the electrodes of the CMUT. The systematic error caused by the poor calibration would give the illusion of a sinusoidal change in S_{11}, even if the sample does not respond. However, the reactance of the sample should change enough around the resonance frequency to give a noticeable local peak or dip in the sinusoidal result curve. Figure 3.11 shows a sketch which illustrates the point.
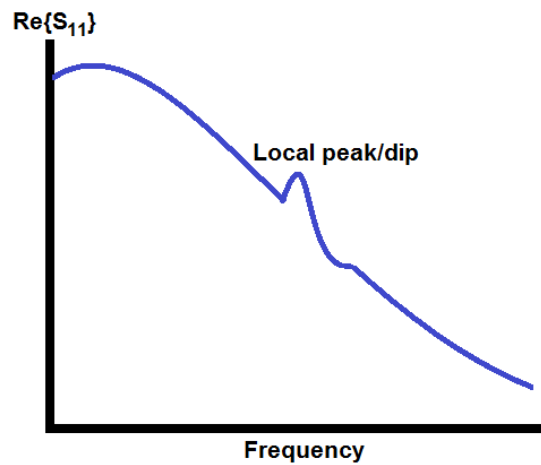
Figure 3.11: Sketch of the expected real part of S_{11} as a function of CMUT excitation frequency. The sinusoidal shape of the curve is a systematic error due to poor calibration, while the local peak and/or dip reveal the resonance frequency. The imaginary part of S_{11} would also have a sinusoidal shape and a local peak and/or dip, but the sine would have a different phase.

4 Experimental setup

This section will describe in words, figures and equations how the interferometer setup works, starting with the optical setup and then moving on to the electrical part. The appropriate background theory on capacitive micromachined ultrasonic transducers (CMUT), heterodyne interferometry and the important acousto-optic modulator (AOM) were presented in sections 3.1, 3.2 and 3.3.

According to ref. [21] there are numerous ways of detecting surface acoustic waves. However, CMUTs often vibrate in the sub-nanometer region at frequencies too high for many systems, so the options are severely limited. Therefore the key to measuring the amplitudes and phases of the CMUT membrane vibrations was in this case to apply heterodyne interferometry. The interferometer available for this project was built by Dr. Hanne Martinussen, during her PhD thesis period 2004-2009 at NTNU, department of electronics and telecommunications. Her research included various measurements on CMUTs, so this project is to some extent built on her accomplishments. In ref.[7], Martinussen and her associates presented a detailed description of the interferometer setup and some selected results. It is in any case appropriate to give a short repetition of the setup description in this report.

4.1 Optical setup

Figure 4.1 illustrates the interferometer and defines the different optical components. The light source of the system is a linearly polarized 532nm diode pumped solid state (DPSS) laser of the type Coherent Verdi V-2. The laser beam is split into a reference and an object arm in a polarized beam splitter (PBS) which transmits horizontally polarized light and reflects vertically polarized light.

As stated in the theory section, heterodyne interferometry is obtained by introducing a frequency shift in one of the interferometric arms. In this case, the frequency shifting is done in the reference arm by the use of two AOMs (ISOMET 1250C). Each of them can change the optical frequency up or down by the same value as their individual acoustical frequency. Two AOMs are used instead of just one because they have a limited bandwidth of 150-250MHz. With the possibility of using one AOM as a frequency downshifter and the other as an upshifter, it is practicable to acquire a net frequency shift of everything between 0MHz and 500MHz. The outgoing beam from the AOMs are then reflected by the mirrors M3, M2 and M1 and partially reflected at the beam splitter (BS) into the photo detector which is an avalanche photo diode (APD) of the type Hamamatsu C5658.
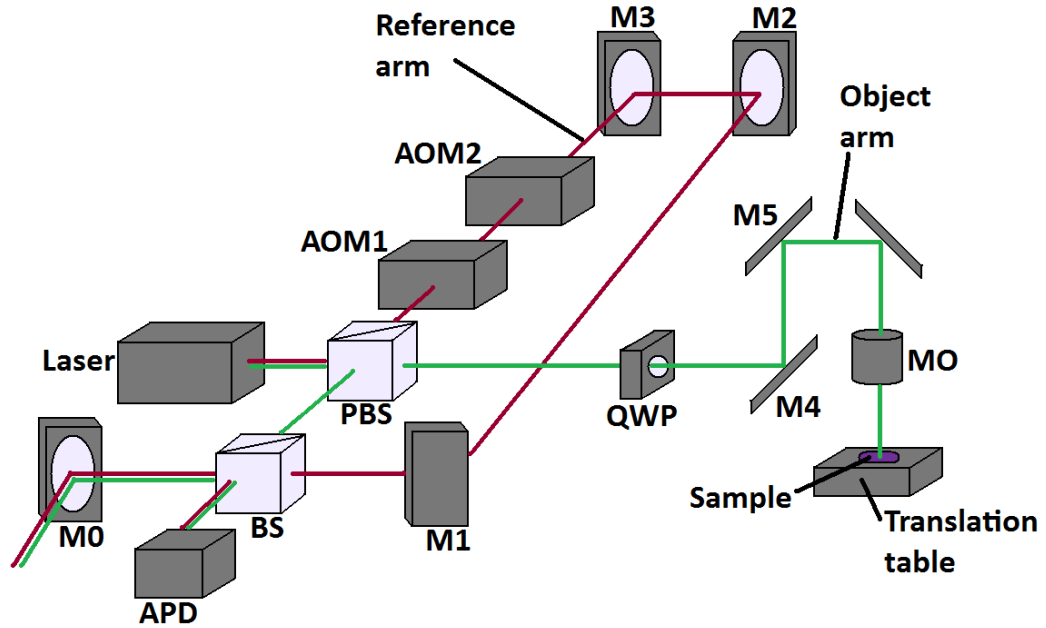
Figure 4.1: Optical setup

When the object beam originates from PBS, it is horizontally polarized when it hits the next component. The quarter wave plate (QWP) transforms the light so that it becomes circularly polarized. The beam is then reflected into a microscope objective (MO) by mirrors M4 and M5 and focused on a very small area of the sample. A motorized xy-translation table (Newport PM500-LW) allows users to move the sample laterally with a resolution of about a tenth of a micron using a computer interface (LabView). Adjustment screws for sample height and tilt are also present on the mounting stage. The object beam is then reflected on the sample and back to QWP through the microscope objective. The reflected light will again have its polarization changed in QWP; the beam will after two runs through the wave retarder have its polarization rotated by 90 degrees with respect to the beam incoming from PBS. That results in this case in linearly vertical polarized light when the beam comes back to PBS. PBS will reflect this rotated beam which now contains information about the sample. The object beam is partially transmitted through BS into the detector, where it interferes with the reference beam. The optical power is then transformed into an electrical current which enters the electrical part of the setup.

The share of the reference and object arms from the BS that do not enter the detector are guided by mirror M0 so that they illuminate the wall in front of the interferometer. It is practical because it lets the user focus the object beam in the picture plane so that the actual CMUTs are visible and enlarged on the wall.

That way it is possible to locate the desired position of measurement and then focus the beam to a small spot after the measurement position has been moved to the centre of the projection. The projection is also useful for aligning the two beams in such a way that they meet.

A photo of the optical setup can be found in figure 4.2.
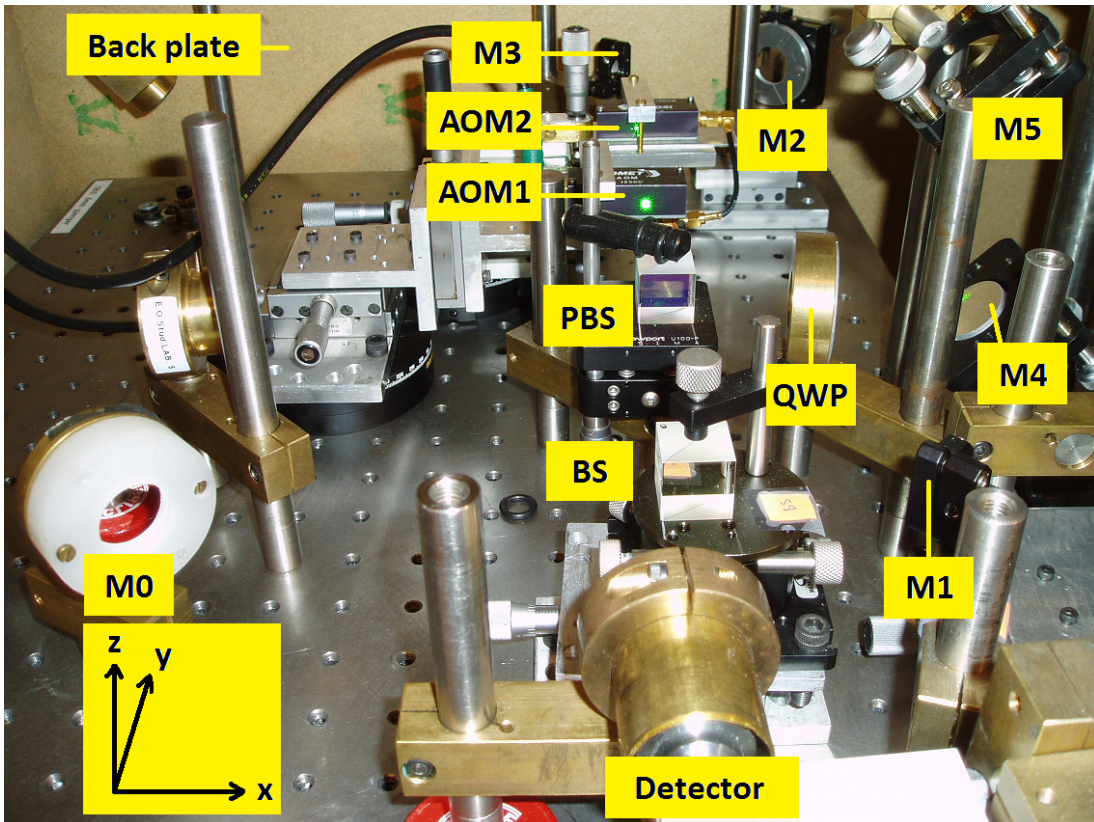
Figure 4.2: Photography of the optical setup

4.2 Electrical setup

The Michelson interferometer in chapter 3.2 is conveniently a simplified version of the interferometer behind the measurements soon to be presented. In other words, the same mathematical expressions which was found in chapter 3.2 are still applicable for the real setup. Two important results from the mathematical reasoning were the expressions for the complex amplitudes R_i and R_n.

$$R_i = 2\sqrt{I_{obj}I_{ref}} \cdot \frac{2\pi a}{\lambda} \mathrm{e}^{j(\phi_a - \phi_{ref} + \phi_{obj})} \tag{4.1}$$

$$R_n = 2\sqrt{I_{obj}I_{ref}} \cdot \mathrm{e}^{j(\phi_{ref} - \phi_{obj})} \tag{4.2}$$

f_a	Frequency of sample vibration
f_m	Combined frequency shift introduced by AOMs
R_i	Complex amplitude of detected intensity at frequency $f_a - f_m$
R_n	Complex amplitude of detected intensity at frequency f_m
I_{ref}	Detected intensity from reference beam
I_{obj}	Detected intensity from object beam
a	Absolute amplitude of sample vibration
λ	Laser wavelength in the medium surrounding the sample
ϕ_a	Phase of sample vibration
ϕref	Phase of reference beam
ϕobj	Phase of object beam

The ratio between these two frequency component amplitudes from the detector signal and λ are all that is required for calculating the absolute amplitude and phase of the vibrating sample according to equations 3.14 and 3.15.

The electrical part of the setup serves the purposes of sample excitation, AOM driving, detection of optical power and extracting the values for R_i and R_n. A sketch of the electrical part of the experimental setup is depicted in figure 4.3. Note that symbols for the ground reference node have been excluded for the sake of simplicity.
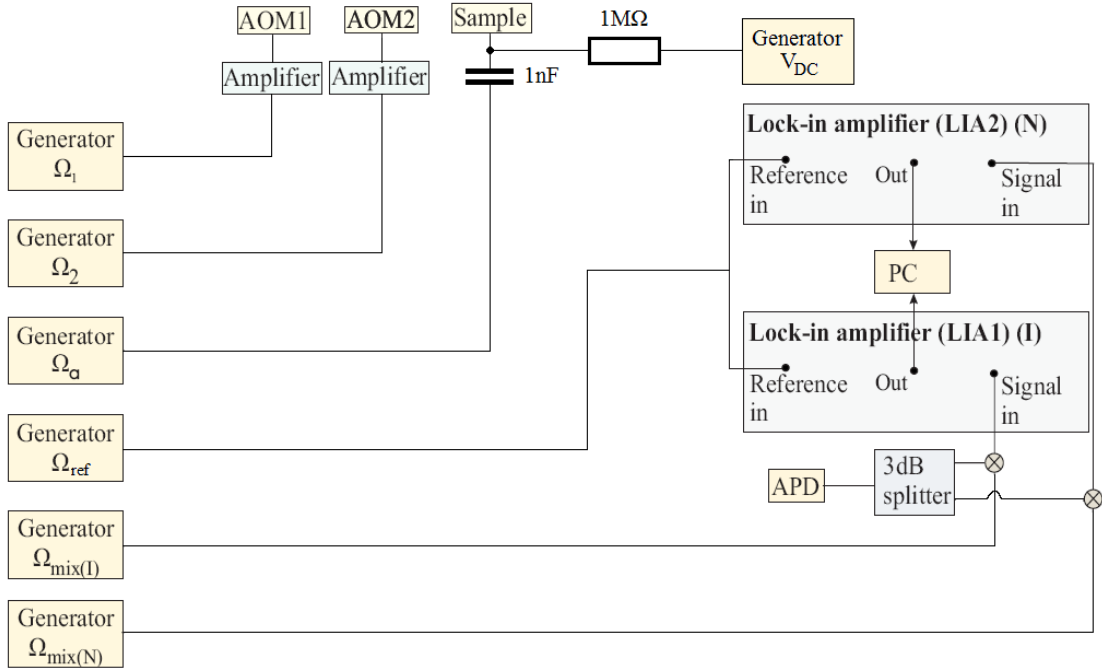
Figure 4.3: Electrical setup[3]

The electrical setup contains seven generators, six of which give AC voltage. The last DC generator V_{DC} provides the sample with a manually controllable bias voltage. All AC generators are synchronized and have the ability to adjust both frequency and amplitude of the output signal. Ω_1 and Ω_2 serves the purpose of driving one AOM each. Generator Ω_a excites the sample with the requested AC voltage and is protected by a 1nF capacitor so that any DC voltage coming from V_{DC} is blocked.

The signals R_i and R_n are to be extracted by two lock-in amplifiers (LIA) of type Stanford Research Systems model number SR830, denoted LIA1 and LIA2 in figure 4.3. A lock-in amplifier can extract a signal with a known frequency from a noisy environment. A clean reference input with the same frequency as the signal is necessary for the device to work. Generator Ω_{ref} provides the LIAs with the reference signal in this particular setup. The LIAs in question can only handle signals up to 100kHz which is not sufficive to measure R_i and R_n directly. Therefore it is necessary to utilize downmixing techniques on the signal originating from the avalanche photo diode (APD) detector.

---

[3]Figure is edited from ref. [7]

The detector signal is first split in a 3dB splitter. The point of that is to send one output from the splitter into LIA1 and the other into LIA2. LIA1 will measure R_i and LIA2 will measure R_n. The reference signal of the LIAs now has a low frequency f_{LIA}, so the frequencies of R_i and R_n must also be mixed down to f_{LIA}. This is done by including two generators $\Omega_{mix(I)}$ and $\Omega_{mix(N)}$ with appropriate frequencies in the setup. $\Omega_{mix(I)}$ and the detector signal mix R_i down to f_{LIA}, while $\Omega_{mix(N)}$ and the detector signal mix R_n down to the same f_{LIA}. Figure 4.4 illustrates the relationship between the frequency components involved in the mixing process.
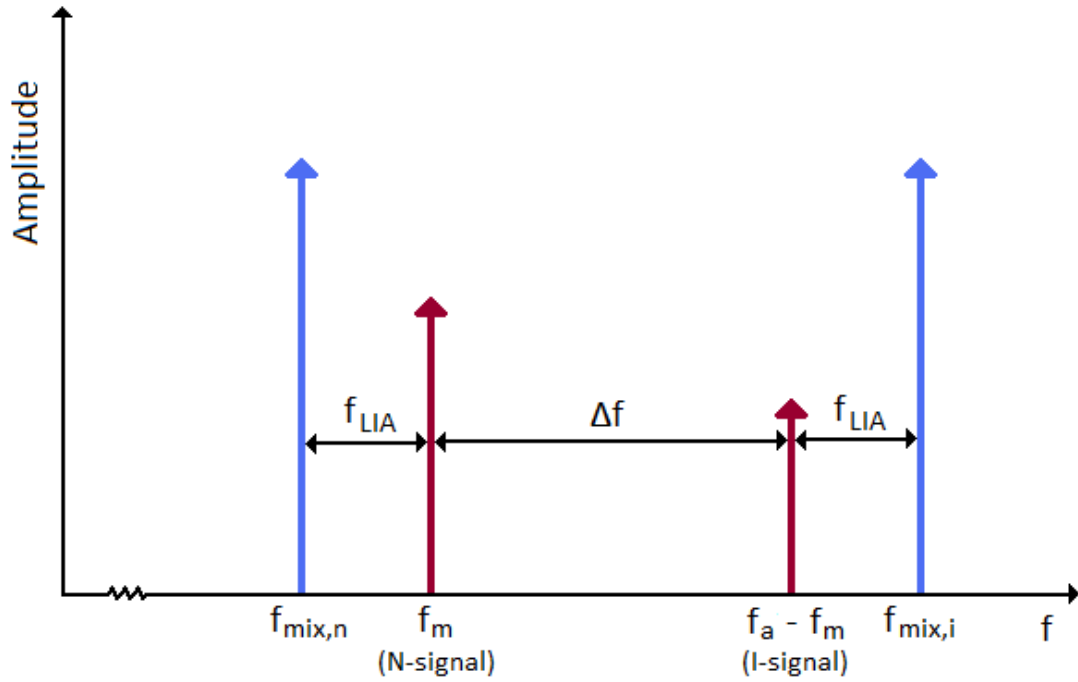
Figure 4.4: Frequency components of detector output, $\Omega_{mix(I)}$ and $\Omega_{mix(N)}$ [4]

---

[4]Figure is from ref. [16]

If local oscillator signals as in figure 4.4 are used, ref. [16] gives the equations 4.3 and 4.4 for the complex amplitudes of the signals entering LIA1 and LIA2. The mixing process has introduced the unknown constants $A_{mix,i}$ and $A_{mix,n}$ and a phase shift in the complex amplitudes of R_i and R_n so that their values are I_i and I_n when entering the LIAs. The ratio between R_i and R_n is still the only value we need. It can be found, provided $A_{mix,i}$ and $A_{mix,n}$ are the same. This can be achieved by using identical mixers and amplitudes of the $\Omega_{mix(I)}$ and $\Omega_{mix(N)}$ generator signals. The phase shifts $\phi_{mix,i}$ and $\phi_{mix,n}$ are uncontrollable and will introduce a random offset in the measured phase. This offset is however not related to any part of the optical setup, so it will remain constant as long as the local oscillators are phase locked to an external reference. The phase-locking fails for a short period of time if the frequency is changed, so phase measurements of the sample vibrations are not presently possible when scanning over a frequency range [16].

$$I_i = 2\sqrt{I_{obj}I_{ref}} \cdot A_{mix,i} \cdot \frac{2\pi a}{\lambda} \cos\left(2\pi f_{LIA}t - \phi_a + \phi_{ref} - \phi_{obj} + \phi_{mix,i}\right) \quad (4.3)$$

$$= A_{mix,i} \cdot \Re\left[R_i^* \mathrm{e}^{j\phi_{mix,i}} \cdot \mathrm{e}^{j2\pi f_{LIA}t}\right]$$

$$I_n = 2\sqrt{I_{obj}I_{ref}} \cdot A_{mix,n} \cdot \cos\left(2\pi f_{LIA}t + \phi_{ref} - \phi_{obj} - \phi_{mix,n}\right) \quad (4.4)$$

$$= A_{mix,n} \cdot \Re\left[R_n \mathrm{e}^{-j\phi_{mix,n}} \cdot \mathrm{e}^{j2\pi f_{LIA}t}\right]$$

I_i	Signal entering the lock-in amplifier 1 in figure 4.3
I_n	Signal entering the lock-in amplifier 2 in figure 4.3
$A_{mix,i}$	Constant dependent on local oscillator amplitude, splitter attenuation, and mixer parameters
$A_{mix,n}$	Constant dependent on local oscillator amplitude, splitter attenuation, and mixer parameters
$\phi_{mix,i}$	Phase of mixing signal
$\phi_{mix,n}$	Phase of mixing signal

It has not yet been explained what value f_m, which is the sum or difference of frequencies of the AOMs, should have. Even if no equations surrounding the interferometer suggest a value, it should not be set randomly. The different components in the electrical setup have their own frequency responses, which leads to different attenuation of signals of different frequency. This implies that the frequency spacing Δf between R_i and R_n should be small to avoid measurement errors. Δf should however be large enough to separate the two frequency components comfortably, so that they do not overlap. A few kHz has been found experimentally to be best value for Δf. We can now make a set of expressions for determination of the frequency settings for the AOMs (f_m) and local oscillators ($f_{mix,i}$ and $f_{mix,n}$) [16], equations 4.5, 4.6 and 4.7:

$$f_m = \frac{1}{2}\left(f_a - \Delta f\right) \tag{4.5}$$

$$f_{mix,n} = f_m - f_{LIA} = \frac{1}{2}\left(f_a - \Delta f\right) - f_{LIA} \tag{4.6}$$

$$f_{mix,i} = \left(f_a - f_m\right) + f_{LIA} = \frac{1}{2}\left(f_a + \Delta f\right) + f_{LIA} \tag{4.7}$$

f_{LIA} Reference frequency of the lock-in amplifiers.
$f_{mix,i}$ Frequency of signal used to mix the detected R_i signal down to f_{LIA}
$f_{mix,n}$ Frequency of signal used to mix the detected R_n signal down to f_{LIA}
Δf Frequency spacing between the detected R_n and R_i signal

5   Gaussian beam width

The theory presented in this section will be used to calculate the minimum width of the laser beam focused onto the sample. This information is interesting to obtain because it gives a clue about how good the spatial resolution of the interferometer is. If the calculations show a small beam width, the interferometer setup may be adapted to measure even smaller acoustic devices than the CMUT. In practice, obtaining the minumum spot size is done by projecting the sample reflection of the object beam on a screen and adjusting the sample height until the projection becomes a spot. This gives good accuracy.

5.1   Useful formulas

The fact that a laser beam has a Gaussian intensity distribution of its fundamental mode TEM_{00} was discovered in the very youth of the laser technology [22]. A Gaussian distribution simplified to a single dimension can according to [23] be expressed as equation 5.1. Changing the arbitrary constants will change the slope, height and/or position of the graph, but it will still have the same fundamental bell-like shape. Note that b must be less than zero because the graph must be concave. The distributions are commonly normalized, which leads to that the integral of the normalized distribution is equal to unity. Figure 5.1 shows some arbitrary Gaussian distributions.

$$f(x) = K \mathrm{e}^{bx^2 + cx + d} \tag{5.1}$$

K Arbitrary constant
x Position variable
b Arbitrary constant
c Arbitrary constant
d Arbitrary constant

The Gaussian profile will be used in order to make the desired calculations possible. Equation 5.2 is an expression for the complex amplitude of a Gaussian distributed field as a function of position [14]. Note that the paraxial approximation [14] was used to obtain the result. The formula is applicable for a focused laser beam, like the beam in this interferometer setup.
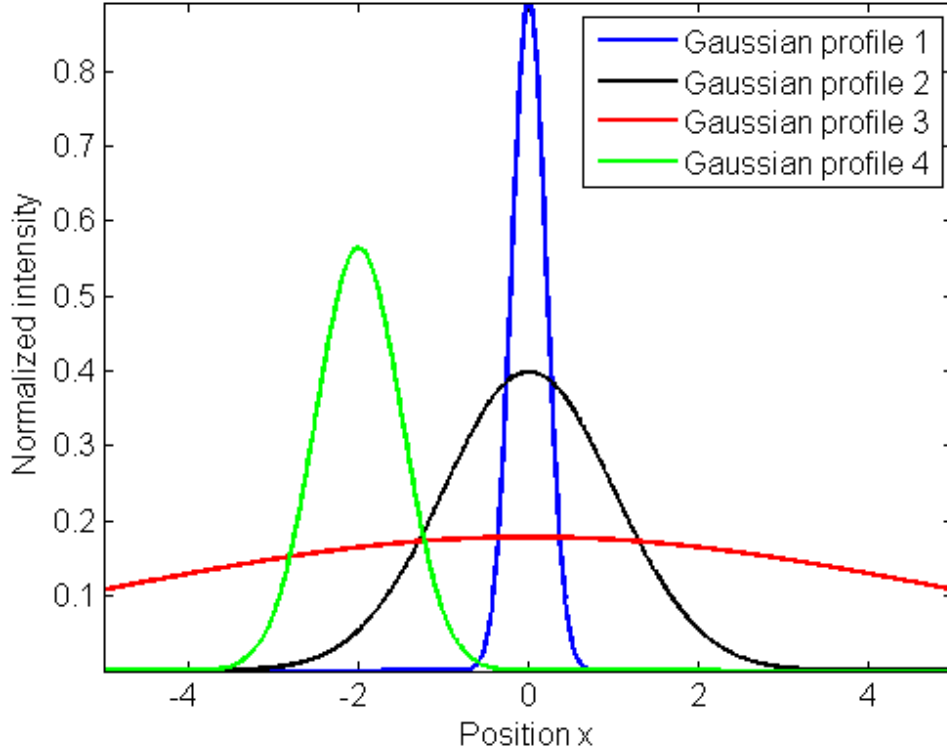
Figure 5.1: Four arbitrary normalized Gaussian distributions

$$U(\vec{r}) = \frac{A_1 W_0}{j z_0 W(z)} \mathrm{e}^{-\frac{\rho^2}{W^2(z)}} \mathrm{e}^{-jkz - jk\frac{\rho^2}{2R(z)} + j\arctan(\frac{z}{z_0})} \tag{5.2}$$

$U(\vec{r})$	Complex field amplitude
$\vec{r}$	Position vector
A_1	Arbitrary constant
W_0	Minimum beam radius
z_0	Rayleigh range
$W(z)$	Beam radius at a position along the z-axis
ρ^2	Simplifying expression, $\rho^2 = x^2 + y^2$
k	Wave number
$R(z)$	Wavefront radius of curvature

$W(z)$ is actually a good measure of the beam radius at a certain point on the axis of propagation, even if the Gaussian field distribution has no abrupt stop as the distance from the beam axis increases. According to [22], the electric field of the beam at a distance $W(z)$ from the beam axis is e^{-1} times the peak amplitude at the axis of propagation. In other words, approximately 86% of the beam power is carried within a circle of radius $W(z)$, [14]. W_0 is known as the beam waist,

i.e. the minimum value of $W(z)$. It is a measure of how narrowly the power of the beam can be focused under certain conditions.

$W(z)$ and W_0 are the most interesting variables of equation 5.2 when calculating the minimum beam width for a laser beam with Gaussian intensity distribution. Expressions for the desired variables are given in ref. [14] and presented here in equations 5.3 and 5.4.

$$W(z) = W_0 \sqrt{1 + (\frac{z}{z_0})^2} \tag{5.3}$$

$$W_0 = \sqrt{\frac{\lambda z_0}{\pi}} \tag{5.4}$$

λ Wavelength

The z_0 parameter is known as the Rayleigh range and is a metric distance. Per definition, the intensity of the beam is 50% of its peak value at a distance of one Rayleigh range from the beam centre [14]. Within this parameter lies the information about the conditions concerning the focusing of the beam. An expression for the Rayleigh range is found in [24] and repeated here in equation 5.5. The numerical aperture is a dimensionless number which characterizes the range of angles in which a system can accept light.

$$z_0 = \frac{\lambda}{\pi NA^2} \tag{5.5}$$

NA Numerical aperture of the focusing interface

5.2 Calculations

The goal of these calculations is to determine the minimum beam radius of the probing laser when propagating in air. The optical system simply consists of a microscope objective focusing the beam down on the non-immersed sample surface. The required parameters of the system is presented in table 5.1.

It is fairly easy to make an applicable formula, it is just a matter of substituting equation 5.5 into equation 5.4 and inserting the known parameters. The formula with its result is stated in equation 5.6.

Table 5.1: Required parameters of the system

Parameter	Value	Description
n_{air}	≈ 1	Refractive index of air
λ_0	532nm	Laser wavelength in vacuum
NA_{MO}	0.45	Numerical aperture of microscope objective

$$W_{0,air} = \frac{\lambda_0}{n_{air}\pi NA_{MO}} \approx 0.38\mu m \tag{5.6}$$

λ_0	Laser wavelength in vacuum
n_{air}	Refractive index of air
NA_{MO}	Microscope objective numerical aperture

0.38μm is a very satisfying result, as there is a distance of several microns across a single CMUT cell. A scan over an entire cell would give a result with high resolution. Even smaller acoustical devices could thus be measured in the same setup without losing too much information. The translation table of the interferometer setup can move with steps of 0.1μm, so the minimum beam width is, however, still the limiting factor of the spatial resolution.

When focusing the beam through air and oil, the spot size would be smaller. However, this size difference is negligable in practice.

6 Sample 1

This section will first present electric and optical measurements performed in air on what is referred to as sample 1. It contains a symmetric CMUT array. Many measurements were done on this sample, but in order to keep this report readable, only the most interesting are included. The results will be presented more or less in a chronological order. That way it is easier to follow the reason for doing the next measurement after seeing the result of the previous one.

The structure is called a symmetric CMUT array due to the shape of the top electrodes, see figure 6.1. In the array, there are 72 cells in one direction and 104 cells in the other. At the end of the columns of the array, the top electrodes are in contact. This means that the whole array should be excited simultaneously when voltage is applied. Each cell's circular membrane has a radius of 5.7μm, thickness of 100nm, and the membrane material is silicon nitride deposited in low pressure. The aluminum top electrodes are 500nm thick, and the gap between the membrane and the bottom electrode is 120nm. The dimensions are fetched from ref. [25].
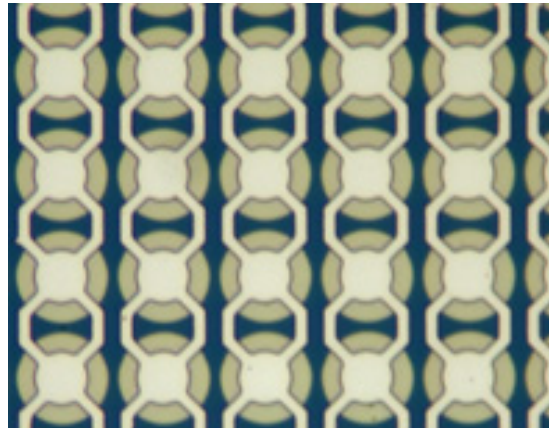
Figure 6.1: Optical microscope photo of the symmetric CMUT array on sample 1, seen from above[4]

---

[4]Captured by PhD student Sigrid Berg

6.1   Electrical measurements

The symmetric CMUT chip was in the start of the semester in the hands of PhD student Sigrid Berg at NTNU. She was conducting electrical measurements on sample 1 with an automatic network analyzer (ANA), type HP 8753E, in order to characterize the frequency response. The measurements are done by connecting the CMUT transmit circuit from figure 3.2 and using the ANA as the AC voltage source. The ANA measures the complex scattering parameter S_{11}, also known as the input reflection coefficient of the network [26]. For more background theory on this subject, please visit section 3.4. When the ANA is calibrated properly, the parameter S_{11} is measured to be larger near the resonance frequency of the CMUTs. Berg's measurement, shown in figures 6.2(a) and 6.2(b), revealed an unexpected behaviour of the frequency response when the CMUTs were biased with -36V. The response has two peaks, which is very rare when measuring an array of alledgedly identical CMUT cells. Network analyzers can only measure the sum of electrically interconnected cells, i.e. not single cells. The sample was thus handed over to the undersigned to look at individual cells with the interferometer. This way it should be possible to determine if all the cells had two peaks in their frequency responses, or if the differences between the cells were large enough to explain the dual peaks.

(a) Real part of input reflection coefficient S_{11}

(b) Imaginary part of input reflection coefficient S_{11}
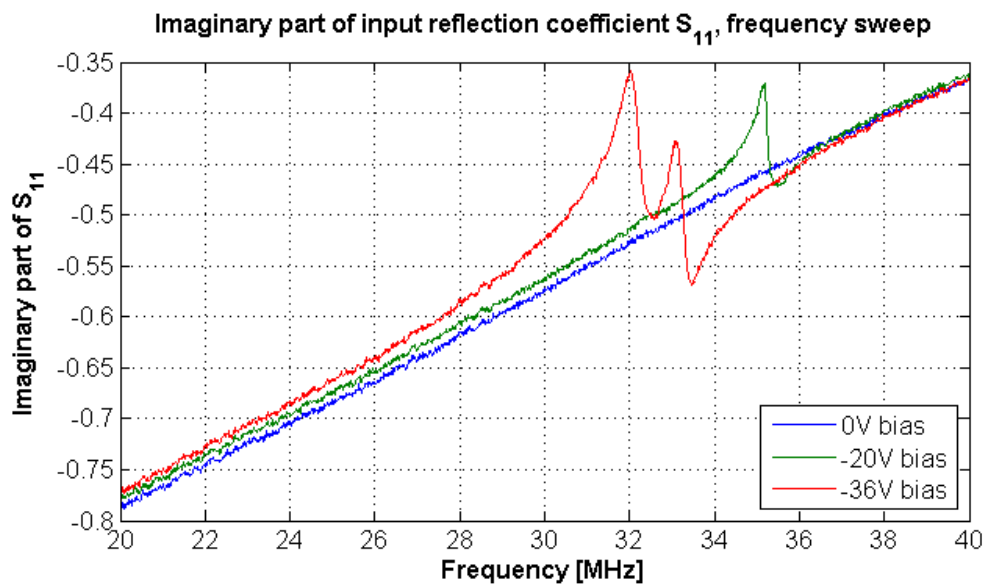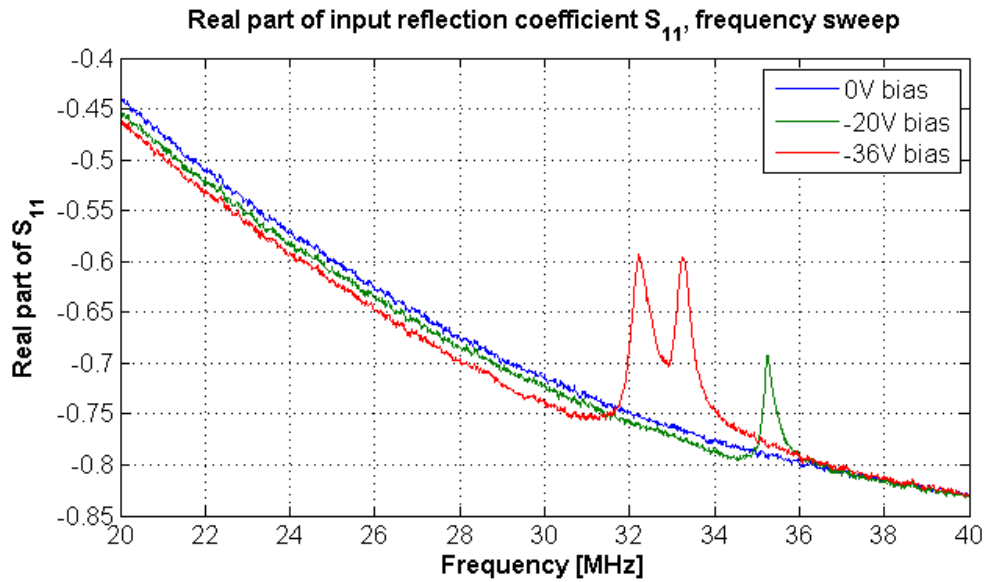
Figure 6.2: Measured input reflection coefficient S_{11} as a function of frequency

6.2   Optical measurements

All measurements presented in this subsection are conducted with the heterodyne interferometer. The laser power was set to 20mW. Frequency scans are done by focusing the laser onto the centre of the CMUT cell in question and exciting it with a range of frequencies. The frequency scans presented here are done with 0.3MHz step between each data point and took between 40 seconds and 1 minute each. 2-dimensional scans are conducted by exciting the CMUT at the resonance frequency and measuring the absolute vibration amplitude and phase at a set of spatial points all over the given area.

The first property to investigate was the frequency response of a set of CMUT cells, i.e. determine the absolute vibration amplitude as a function of excitation frequency. The behaviour of the S_{11} graphs in figures 6.2(a) and 6.2(b) could then hopefully be better explained. It was decided to scan the 9 cells closest to each corner of the array and 9 cells in the middle of the array, a total of 45 cells. This was to include possible edge effects and to get a representative selection of CMUT cells. The results are presented in figure 6.3.
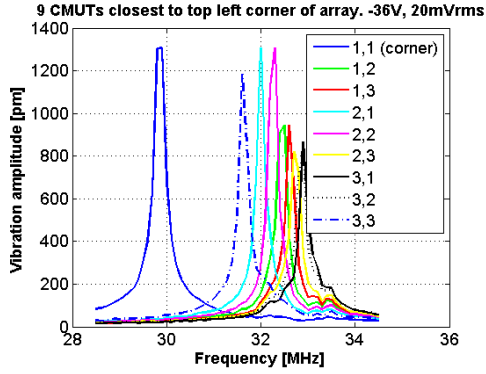
(a) Frequency responses of the 9 cells closest to the top left corner of the array
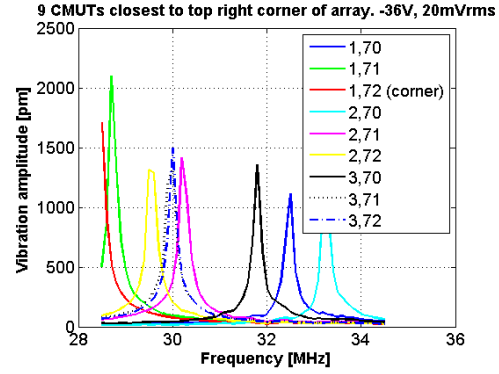
(b) Frequency responses of the 9 cells closest to the top right corner of the array
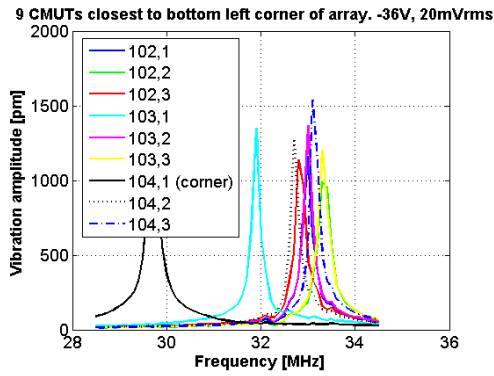
(c) Frequency responses of the 9 cells closest to the bottom left corner of the array
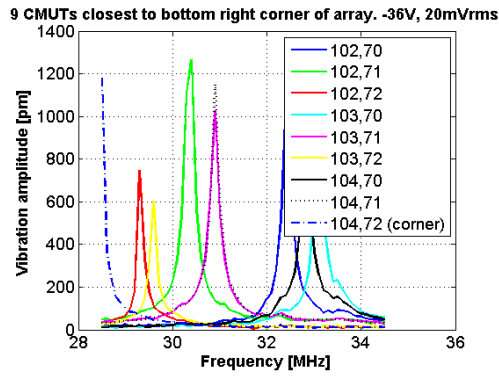
(d) Frequency responses of the 9 cells closest to the bottom right corner of the array
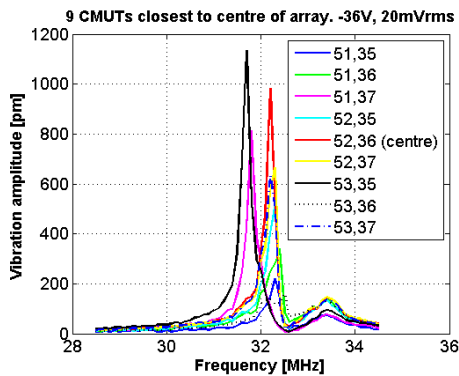
(e) Frequency responses of the 9 cells closest to the centre of the array
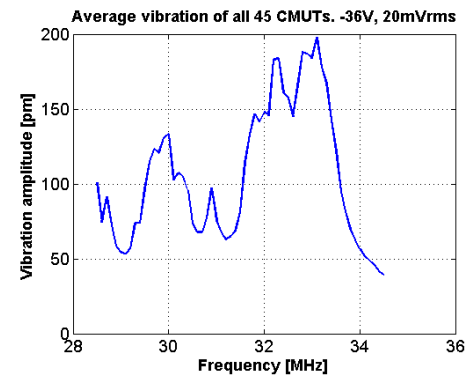
(f) Average frequency response of all the 45 cells

Figure 6.3: Frequency responses of 45 cells when excited with 20mV_{RMS} and -36V bias voltage. The numbers in the graph legends denote the location of the cell in the array, where (1,1) is the top left cell. The x-direction is downwards and the y-direction is towards the right of the array.

During the frequency scans in figure 6.3 it became clear that the resonances were drifting along the frequency axis as a function of time. It was not known what this phenomenon could be, so before each scan the excitation voltages and the laser were turned off for 5 minutes. The scans were done immediately after turning the stimulis back on in order to give the sample close to the same starting conditions. This seemed to give nearly repeatable results.

It was decided to investigate the drifting resonance frequencies further. The same method as in the last paragraph was used in order to recreate the same conditions for each scan of the sample. A number of frequency scans were then conducted while keeping track of how long the CMUT voltages and the laser had been turned on. Figures 6.4, 6.5 and 6.6 show the results of the scans when looking at three different cells in the array. It was also necessary to determine if the drifts not only were a function of position, but also applied DC voltage. The corner cell (104,1) was tested with both $-36V$ and $-20V$ bias, see figures 6.6 and 6.7. (104,1) denotes the location of the cell in the array, where the first coordinate denotes the cell number in the x-direction and the second coordinate represents the y-direction.
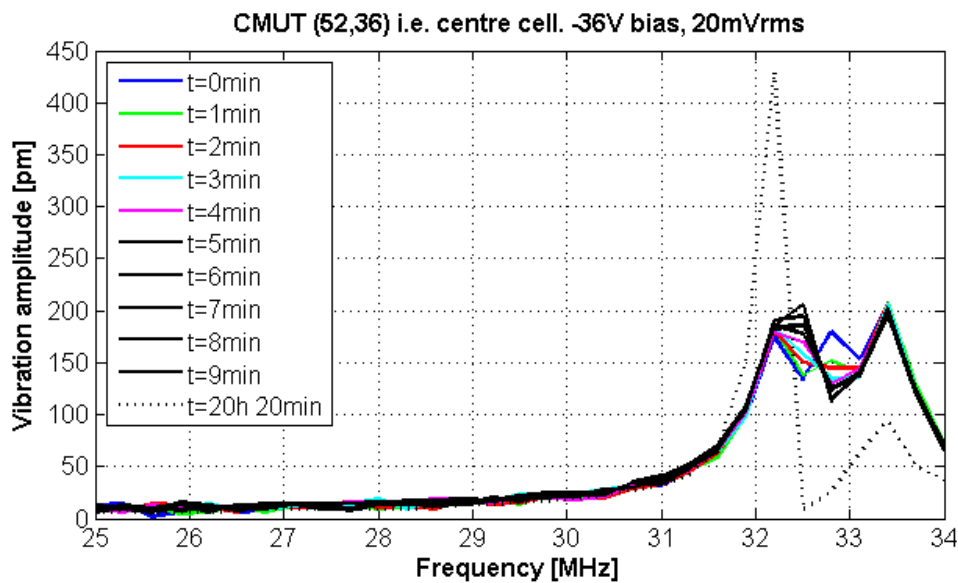
Figure 6.4: Frequency scans of array centre cell (52,36) with $-36V$ bias and a $20mV_{RMS}$ AC component applied
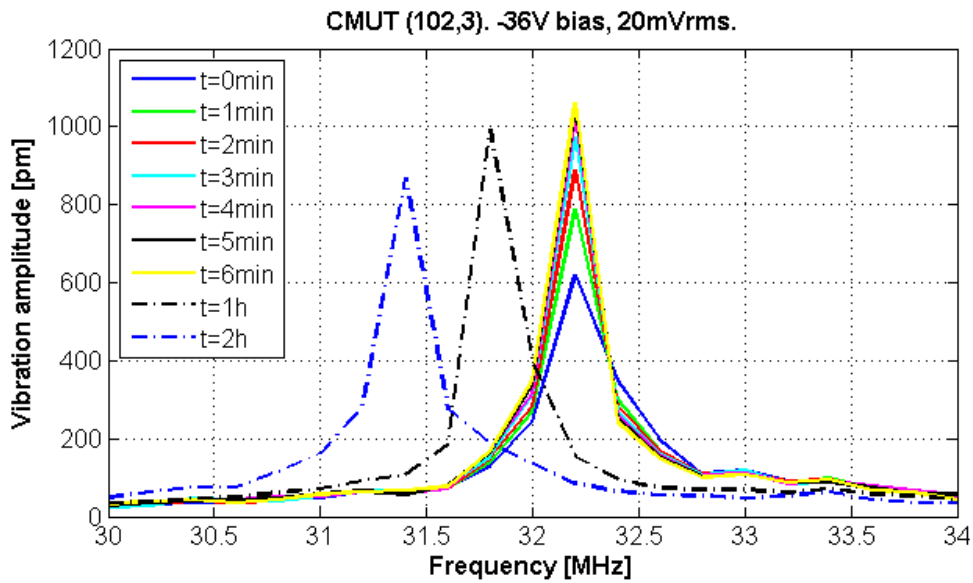
Figure 6.5: Frequency scans of array cell (102,3) with −36V bias and a 20mV$_{\text{RMS}}$ AC component applied
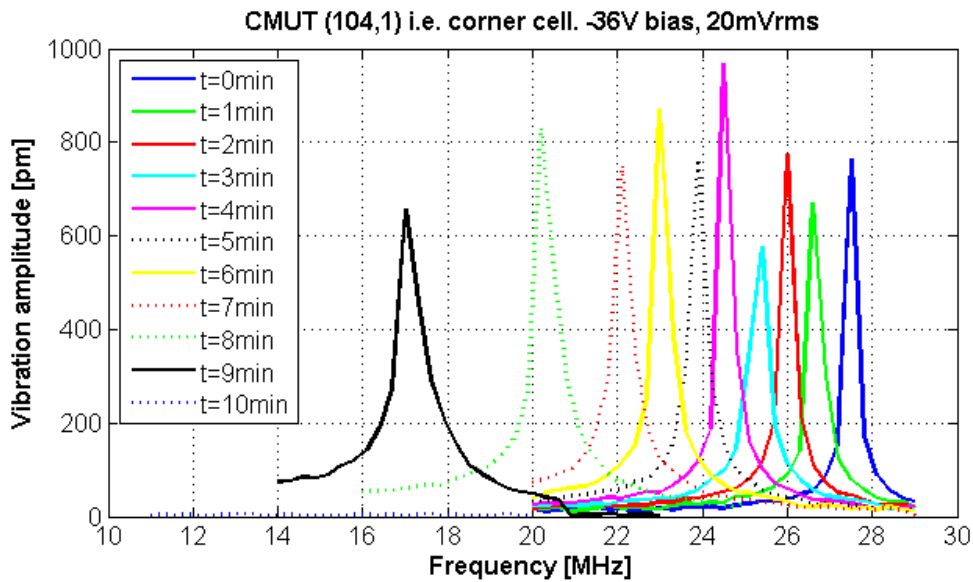
**Figure 6.6:** Frequency scans of array corner cell (104,1) with −36V bias and a 20mV$_{\text{RMS}}$ AC component applied

43
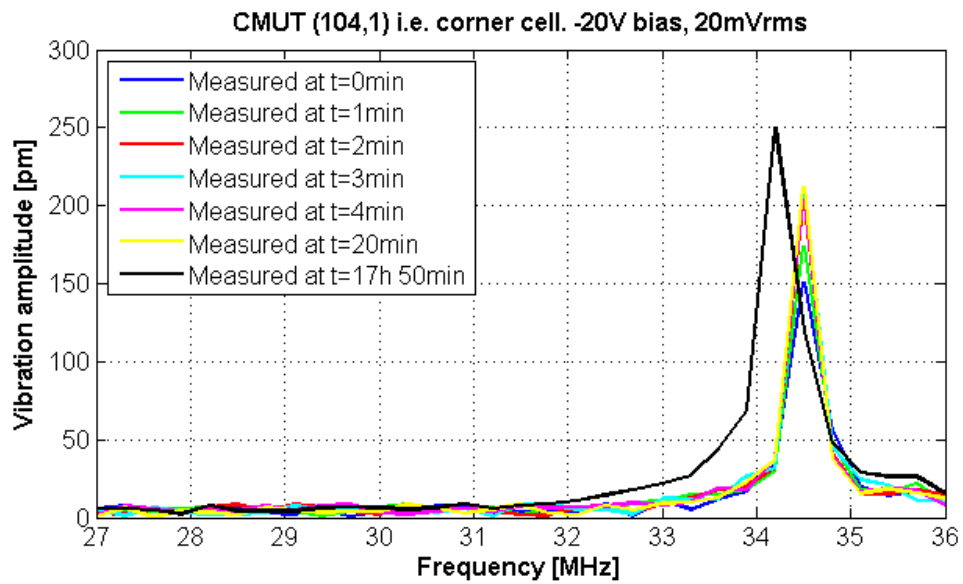
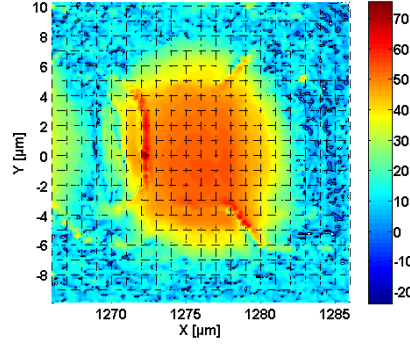**Figure 6.7:** Frequency scans of array corner cell (104,1) with -20V bias and a 20mV$_{\mathrm{RMS}}$ AC component applied

The resonance frequency of the cell (104,1) seems to be vanishing after about 10 minutes of activity according to figure 6.6. The same scan as in this figure was repeated. When the resonance could no longer be observed, the bias voltage was turned off for 20 seconds. Then the voltage was switched on and a new scan was made to observe the CMUT cell vibrations coming back to life. The result is depicted in figure 6.8.
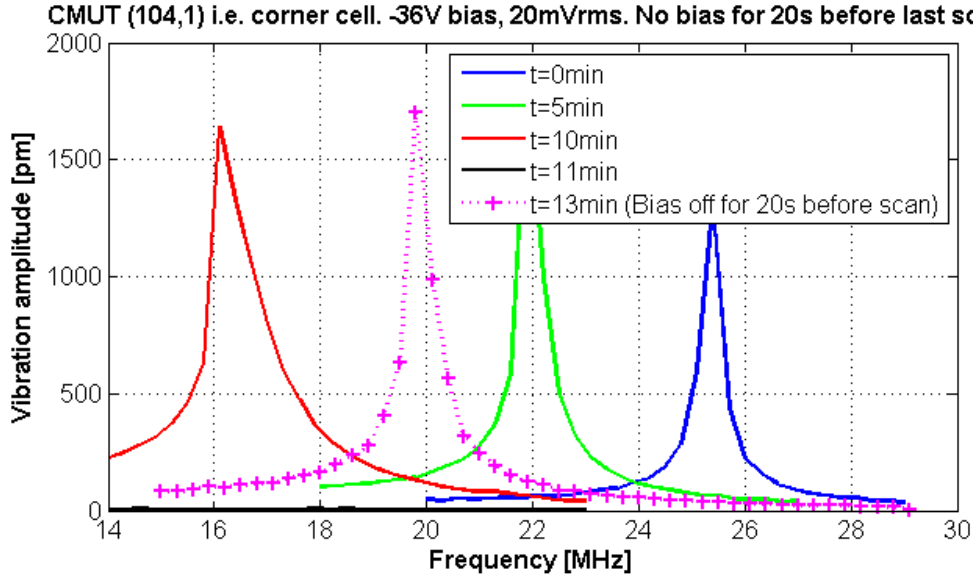
Figure 6.8: Frequency scans of array corner cell (104,1) with −20V bias and a 20mV$_{\text{RMS}}$ AC component applied. Bias turned off for 20 seconds before the last scan.

The level of bias voltage definitely has an impact on how fast the resonance frequency is drifting. Next, it was suggested to reverse the polarity of the bias to see if this had anything to do with the velocity of the drifts. Tests were conducted on the corner cell (104,1) with −28V and +28V bias. The results are given in figures 6.9 and 6.10.
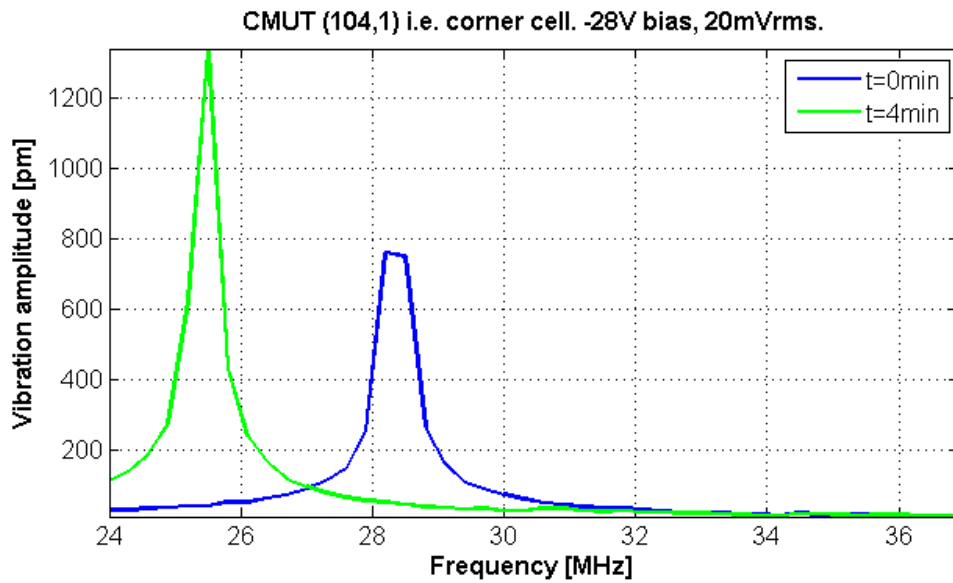
Figure 6.9: Frequency scans of array corner cell (104,1) with −28V bias and a 20mV_RMS AC component applied.
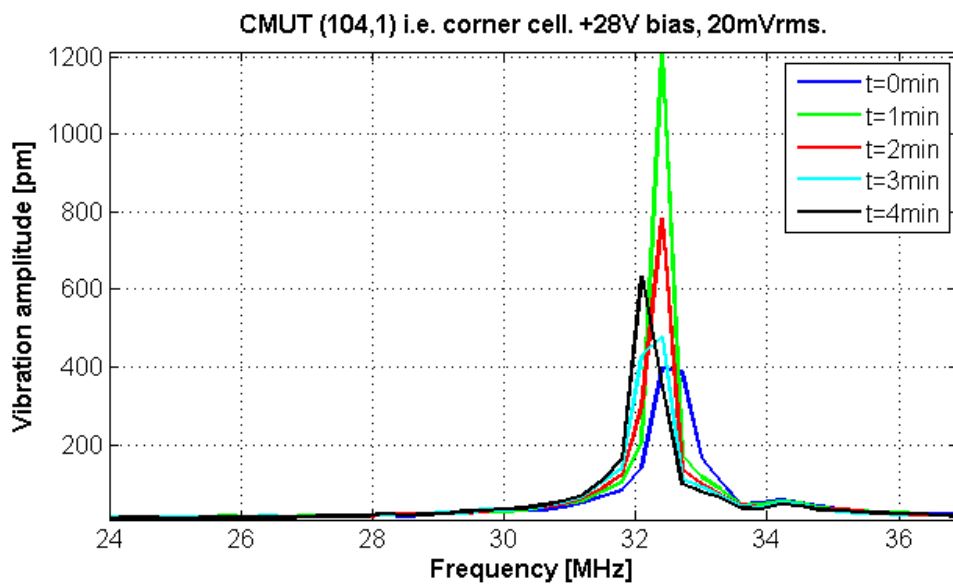
Figure 6.10: Frequency scans of array corner cell (104,1) with +28V bias and a 20mV_RMS AC component applied.

It was at this point solidly established that the drift in resonance frequency was influenced by the bias voltage. The rate of the drift also differed from cell to cell. It was therefore decided to take 2-dimensional scans of the corner cell (104,1) and the centre cell (52,36) in order to look for differences in the vibration pattern which may explain why one cell's resonance drifts more than the other. The measurement of the corner cell could not be done at a higher bias voltage than -20V because the resonance peak would drift away during the scan, rendering the result inreliable. The centre cell was subjected to -36V bias. The results of the 2-dimensional scans are shown in figures 6.11 and 6.12. Note that the area between each data point has been interpolated for a better illustration. The figures contain information about vibration amplitude, phase and the amplitude of I_n from equation 4.4. I_n is a good measure of the signal strength and thus the optical reflectivity at a certain measurement point.
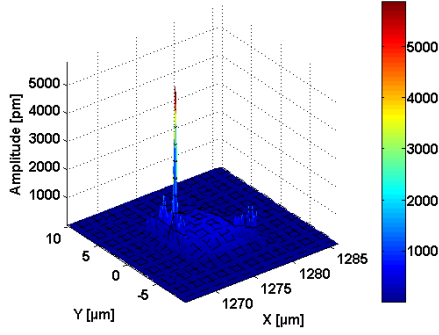
(a) Colours, contour and height represent absolute vibration amplitude. The unit of the colour bar is picometers.

(b) Colours and contour denote absolute vibration amplitude in a logarithmic scale. The unit of the colour bar is decibel picometers.
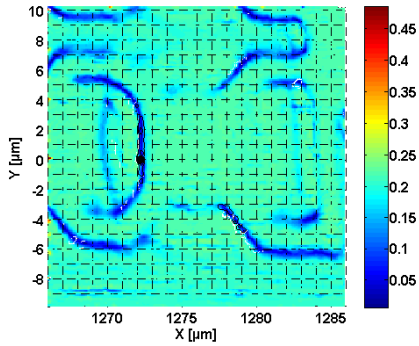
(c) Colours represent reflectivity (amplitude of I_n), and contour denotes absolute vibration amplitude. The unit of the colour bar is volts.
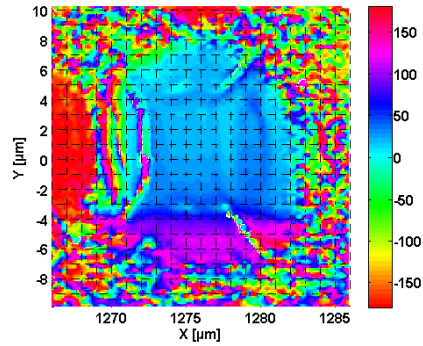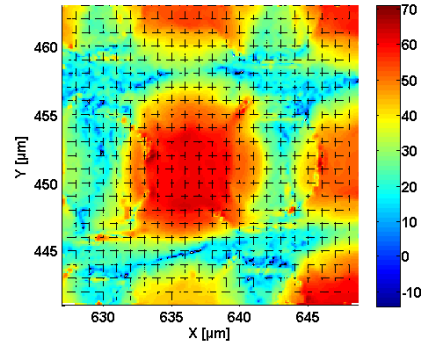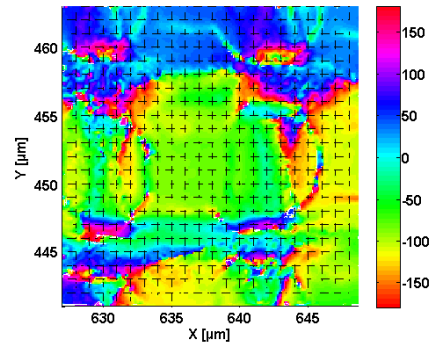

(d) Colours represent the phase of the vibrations, and contour shows absolute vibration amplitude. The unit of the colour bar is degrees.

Figure 6.11: Array cell (104,1) measured at its resonance frequency 34.5MHz when excited with -20V bias and 20mV$_{RMS}$
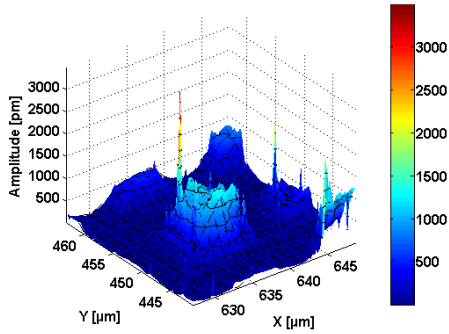
(a) Colours, contour and height represent absolute vibration amplitude. The unit of the colour bar is picometers.

(b) Colours and contour denote absolute vibration amplitude in a logarithmic scale. The unit of the colour bar is decibel picometers.
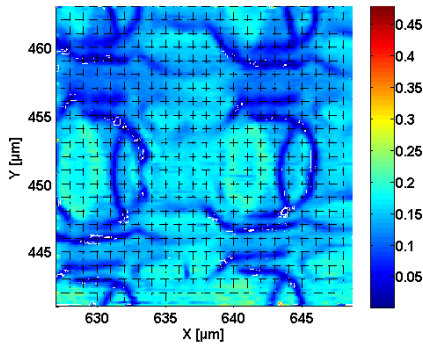
(c) Colours represent reflectivity (amplitude of I_n), and contour denotes absolute vibration amplitude. The unit of the colour bar is volts.

(d) Colours represent the phase of the vibrations, and contour shows absolute vibration amplitude. The unit of the colour bar is degrees.

Figure 6.12: Array cell (52,36) measured at its resonance frequency 32.1MHz when excited with -36V bias and 20mV$_{\text{RMS}}$

6.3   Discussion

6.3.1   Spread resonance frequencies

Figure 6.2 shows the frequency response of the input reflection coefficient S_{11}. When the sample had a bias of $-36V$ the response showed two distinct peaks with a spacing of 1.1MHz, which is very rare for those CMUTs. The main objective for measuring sample 1 optically was to be able to explain this phenomenon. The electrical measurement probed the whole array simultaneously since the top electrodes of this particular CMUT prototype are connected. Hence, the resulting S_{11} frequency response is strongly correlated to the sum of the vibrations of every cell in the array as a function of excitation frequency. Performing interferometric measurements of the absolute vibration amplitude of the 7488 cells in the array at a range of frequencies would give the opportunity of looking at the characteristics of each cell to determine if the dual peaks are inherent in every CMUT. It would also be possible to calculate the sum of the vibrations of the entire array at each tested frequency to check the result up against the electric measurement. However, this would result in unmanageable amounts of data, so it was decided to scan cells from different areas of the array to get a representative selection.

After doing 45 frequency scans of individual cells in the CMUT array it became clear that the two peaks did not represent two distinct modes of vibration common for every cell. In other words, all the cells had one single resonance frequency within the frequency range the CMUT was meant to operate. One might question this statement after looking at figure 6.4. In this figure, the frequency response of cell number (52,36) has two peaks at about the same vibration amplitude. This phenomenon was observed only for this particular cell, however, and does not affect the total frequency response in any mentionable manner. Figures 6.3(a)-(e) show that the resonance frequencies of the 45 measured cells are scattered over an area of about 5MHz, which is a wider band than the electric measurement would suggest. Looking closely at the graphs in figures 6.3(a)-(e), one notices that the cells close to the edge of the array have a lower resonance frequency than the ones closer to the centre.

In figure 6.3(f) all the 45 cells' vibrations have been averaged for each measured frequency. The peak at 30MHz is not found in the scan of S_{11}. This is probably because this peak mostly originates from the resonances of the edge cells, and the ratio of measured edge cells was much larger in the optical scans than in the electrical scan of the whole array. In the optical measurements, 20 of 45 cells were located at the edges, while in the whole array 350 of 7488 cells are on the edges. Thus the resonances of the edge cells may have been hard to see in the electric scan. The two peaks at 32MHz and 33MHz are in any case visible on both the electric scan and the average of the optical measurements. This fact means that the sample had the same conditions in both the electric and optical measurements, and validates the results.

6.3.2   Temporal drift

It was established that the cells within the array have different resonance frequencies, but it was decided to take the measurements one step further. This was because some of the resonance frequencies seemed to be shifting as a function of how much time the sample had been under the influence of applied bias voltage. Figures 6.4, 6.5 and 6.6 indicate that the rate of the drift is also dependent on where the cell is located in the array. Figure 6.7 shows that the drift is a function of the level of applied DC voltage as well. The reason for these resonance drifts is not completely clear. Three theories are outlined.

The first theory is that the adhesion between the membrane and the substrate is poor at the edges of the array. This could have happened when the chip was under processing. A low level of adhesion could result in an effective membrane diameter being larger on the cells near the edge, which would be equivalent to a larger area of vibration and thus give a lower resonance frequency. At high bias voltages, this effect would be enlarged.

Another theory is directed towards the materials of the CMUT chip. The top electrode could be subjected to strong enough electrostatic forces to induce creeping/yielding of the aluminum when voltage is applied. This could make the frequency response of the cells quite unpredictable and explain the strange measurement results.

The last and most supported theory is based on charges. Silicon nitride is the membrane material of the CMUT and is a good electrical isolator. However, ref. [28] has submitted that charges may be trapped in the silicon nitride layer. Even a small leakage current from an electrode could be enough to accumulate charges in the membrane [29]. The effects of such an accumulation in a CMUT membrane have already been investigated in ref. [30], where the author showed that the buildup of charge would increase the electric potential difference between the

electrodes. In the eyes of the electrodes, this would be the same as an increasing bias level. In turn, that would lead to the membrane bending towards the bottom electrode, thus making the resonance frequency drift along the frequency axis until the membrane finally collapses. Ref. [30] also suggests that the buildup of charge would go exponentially faster with a linearly increasing applied bias voltage. This explains why the resonance frequency in figure 6.7 (-20V bias) shifted much slower than in figure 6.6 (-36V bias). The charges entering the membrane could come from either the top or the bottom electrode. Figure 6.13 illustrates charges coming from the bottom electrode and figure 6.14 shows charges coming from the top electrode.

The latter theory is supported by the results in figure 6.8 where the bias was applied until the membrane collapsed. Turning the bias off for 20 seconds probably allowed some of the charges to recombine into electron-hole pairs, decreasing the potential difference between the electrodes. The last scan shows that the membrane has detached from the bottom electrode and is vibrating again, but still with a higher effective DC voltage than the bias which is applied by the generator.

Figure 6.10 illustrates a measurement series on the cell which seems to have the fastest drift of resonance frequency in the earlier scans. The difference in this particular measurement is that the polarity of the voltage has been reversed, applying a bias of $+28$V instead of -28V, as in figure 6.9. Clearly, the drift moves much slower with a positive voltage polarity. It is assumed that the reason for this is that electrons and holes have different mobilities. Put in other words, electrons move easily into the membrane and get trapped there at a negative bias voltage, while holes have a harder time moving into the membrane when the voltage is positive.
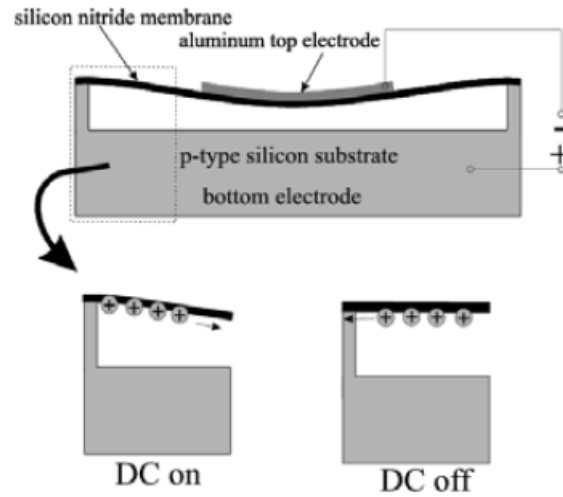
Figure 6.13: Possible charging mechanism; charges entering the membrane from the doped silicon substrate [27]
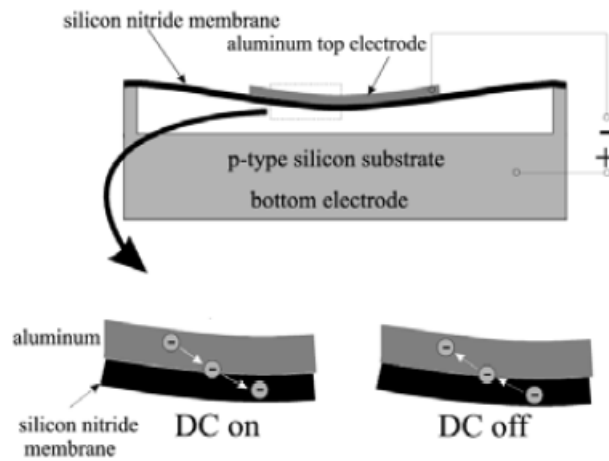
Figure 6.14: Possible charging mechanism; charges entering the membrane from the aluminum top electrode [27]

6.3.3 Vibration patterns

Two 2-dimensional scans were conducted on two cells operating at their resonance frequencies, one at the corner of the array and another in the middle. The corner cell had shown a large frequency drift, while the other seemed quite stable. The purpose of the measurement was to identify visible defects which may explain why the two cells had different properties. The results of the scans are shown in figures 6.11 and 6.12. Subfigures 6.11(c) and 6.12(c) illustrate the optical reflectivity of the measured areas and could give an indication if the cells were damaged physically. However, it is not possible to see any flaws from the reflectivity plots. The amplitude plot of the corner cell in figure 6.11(a) shows a large spike. The high vibration amplitude at the spike is probably not real. Due to the difference in height between the electrode and the membrane, the boundary conditions of the object beam may be unclear at the border between the two planes. This phenomenon could give unwanted diffraction and distort the signal at the detector. Figure 6.11(b) represent the same data as in figure 6.11(a), but is plotted logarithmically for better visibility. The vibration amplitude plots do not show any indication as to why the resonance frequency might drift more for one cell and less for the other. Subfigures 6.11(d) and 6.12(d) indicate the phase of the vibrations. The one thing which may indicate unwanted behaviour of the corner cell is seen in its phase plot. The pink areas on the cell vibrate slightly out of phase with the rest of the membrane. It is unknown if this is a measurement artifact or if the cell is damaged in this out-of-phase area.

One might ask why the neighbouring cells are vibrating out of phase with respect to each other when they are excited by the same AC signal. The reason is simply that the cells have different resonance frequencies, and thus their phases differ as well. Cells have different resonance frequencies mainly because fabrication is never perfect. Even a small difference in the geometrical and material properties will affect the location of the resonance frequency for each cell.

7   Sample 2

This section comprises the results and appropriate discussion on the second sample which we call sample 2. The chapter is structured the same way as the section on the symmetric sample. First, some network analyzer results are presented with the sample positioned in air, followed by optical measurements done in air and in oil. Next, another electrical measurement will be shown in order to make a comparison of the same measurement done before the sample was immersed in oil. Lastly, there will be a discussion of the results.

This prototype is an older CMUT version. Figure 7.1 shows a photo taken of this sample through a microscope. There are fewer cells on this array, 52 in one direction and 36 in the other. The cell columns are interconnected at the top electrodes and each row is interconnected to one of its neighbouring rows. The cells have circular membranes with a radius of 11.4μm, thickness of 100nm, and the membrane material is silicon nitride deposited in low pressure. The aluminum top electrodes have a thickness of 500nm, and the cavity between the membrane and the bottom electrode is 120nm. The dimensions are collected from ref. [25].
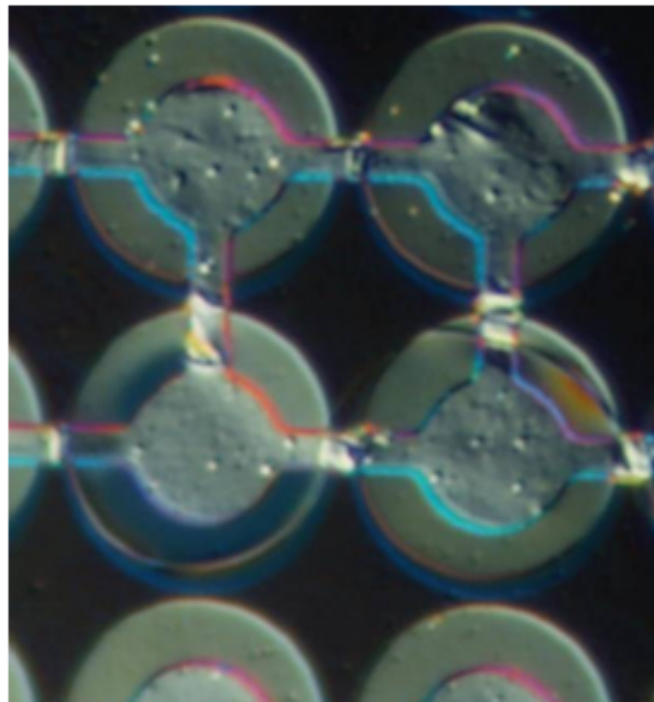
Figure 7.1: Optical microscope photo of the CMUT array on sample 2, seen from above

The sample was unused before these measurements were taken, in other words no voltage had ever been applied over the electrodes. This presented a unique opportunity to observe any phenomena which could change the characteristics of the CMUT during the first few uses. The second incentive for measuring on this type of CMUT is to be able to compare the frequency responses of the CMUT when surrounded by air and immersed in a liquid. This had never been done before with the optical setup. Finally, another electrical measurement was performed in the network analyzer after a cleaning session to get an idea of the durability of the CMUT chip.

7.1 Electrical measurements 1

Sample 2 was connected to its transmit circuit and hooked up to the automatic network analyzer (ANA). Then three different bias voltages were applied in a rising fashion, and the scattering parameter S_{11} was measured in the frequency range 5MHz-20MHz. The AC excitation was at a level of 10mV_RMS. The measurement results can be viewed in figure 7.2.
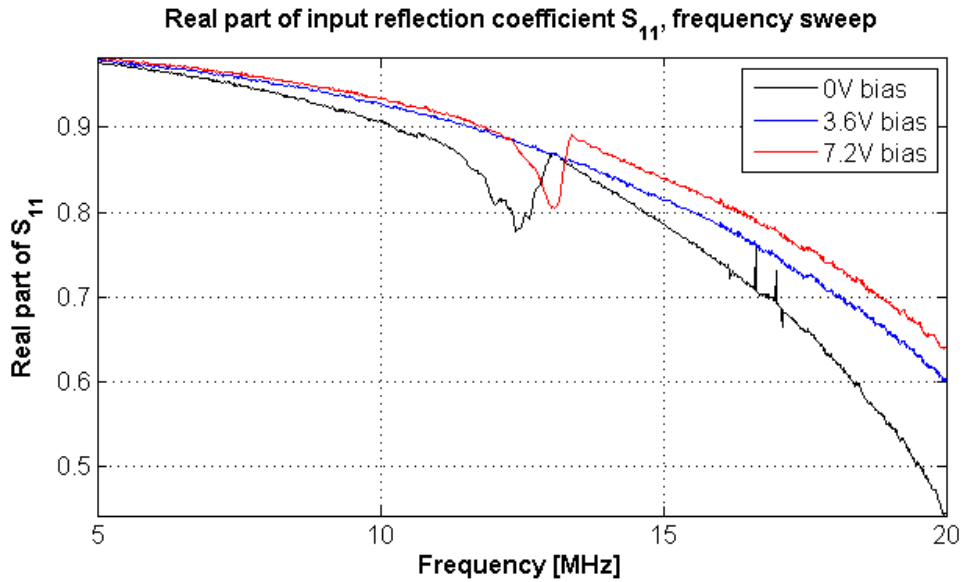
(a) Real part of input reflection coefficient S_{11}
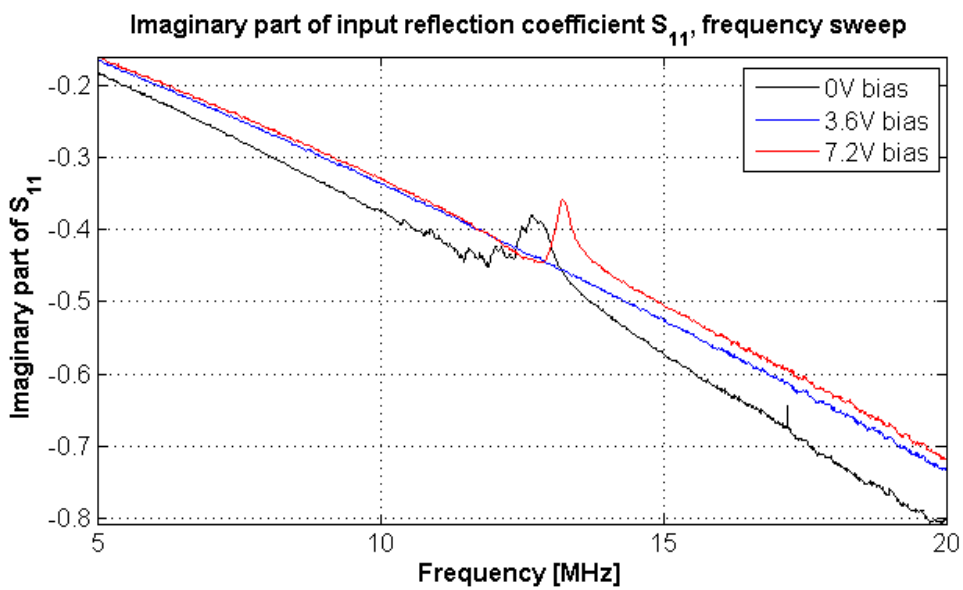
(b) Imaginary part of input reflection coefficient S_{11}

Figure 7.2: Measured input reflection coefficient S_{11} as a function of frequency. The sample was not immersed.

7.2 Optical measurements in air

The first optical measurement series to be conducted was frequency scans of a single and arbitrary CMUT cell. The plan was to increase the bias voltage in increments while measuring the frequency response for each bias level. The highest bias was 12V, which should be enough to collapse the membrane. After completing this set of measurements the series was repeated two times to see if the collapse changed the characteristics of the frequency response. The results are shown in figure 7.3.
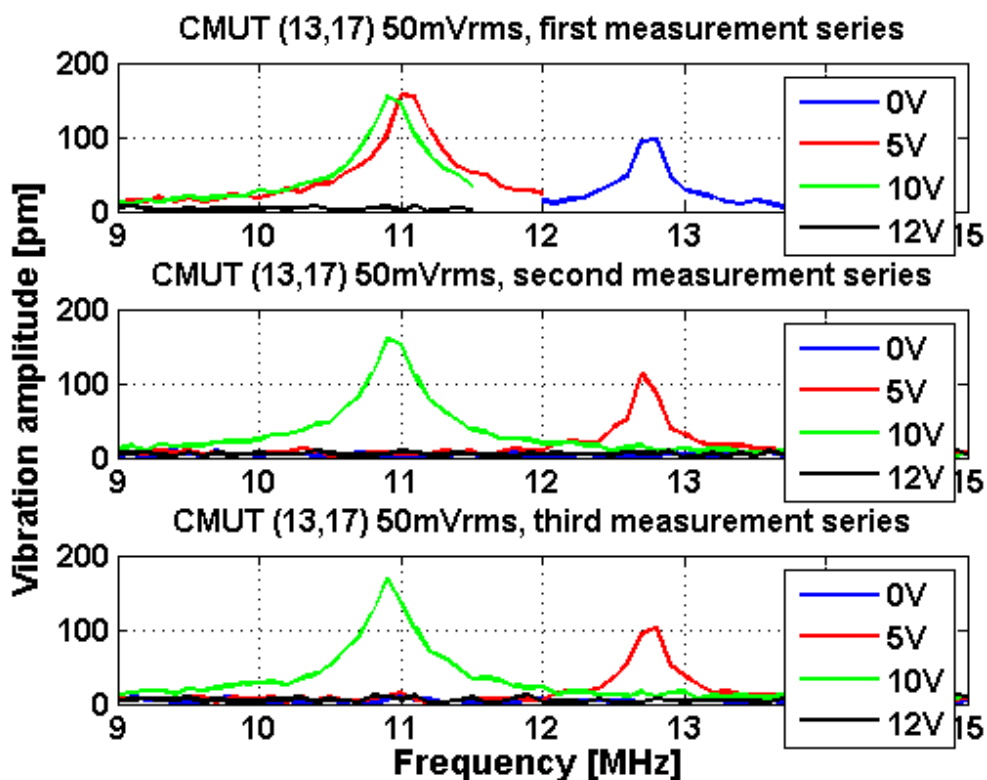
Figure 7.3: Frequency scans of array cell (13,17) with increasing bias increments and an AC excitation of 50mV$_{\text{RMS}}$.

After observing the drift in resonance frequency of the symmectric sample in section 6, it became clear that it was necessary to check if this phenomenon could cause a problem for the measurements on sample 2. Hypothetically, charges accumulated by the bias would result in increasing electrostatic attraction forces between the electrodes. This would bend the membrane gradually towards the substrate while changing the resonance frequency. A resonance frequency being dependent on how long the bias had been on, would make the larger and more time consuming measurements invalid. To test whether or not resonance drifting

was the case, frequency scans were done at different times on the array cell (21,17) while keeping a relatively high bias of 10V. Charges may still be trapped in the CMUT even after the bias voltage is switched off. They would be pulling on the membrane and possibly creating the conditions for a resonance peak in the frequency response before they have the time to dissipate. The bias was thus turned off, and a new measurement was done immediately. This was done to look for a resonance frequency which could only exist if the electrodes have a charge difference between them; an effective bias voltage. The result of this measurement series are presented as graphs in figure 7.4.
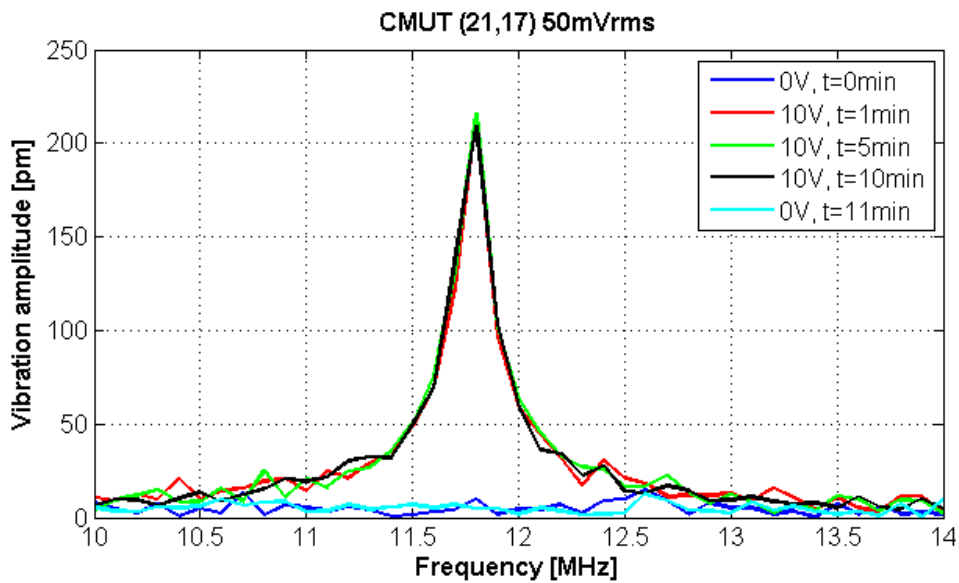
Figure 7.4: Frequency scans of array cell (21,17) with two different different bias levels and an AC excitation of 50mV$_{\text{RMS}}$.

Now that it is clear that cell (21,17) does not have a flaw causing the resonance frequency to drift, time consuming measurements could be conducted without the concern of changing conditions. It was decided to make the frequency scan of the cell more thoroughly, this time with a wider frequency range and several measurement points along a line crossing the CMUT. In other words, measuring was made on several x-coordinates ranging over the CMUT membrane while keeping the y-coordinate fixed. The result is plotted in figure 7.5. Different colours indicate strong or weak vibration amplitudes.
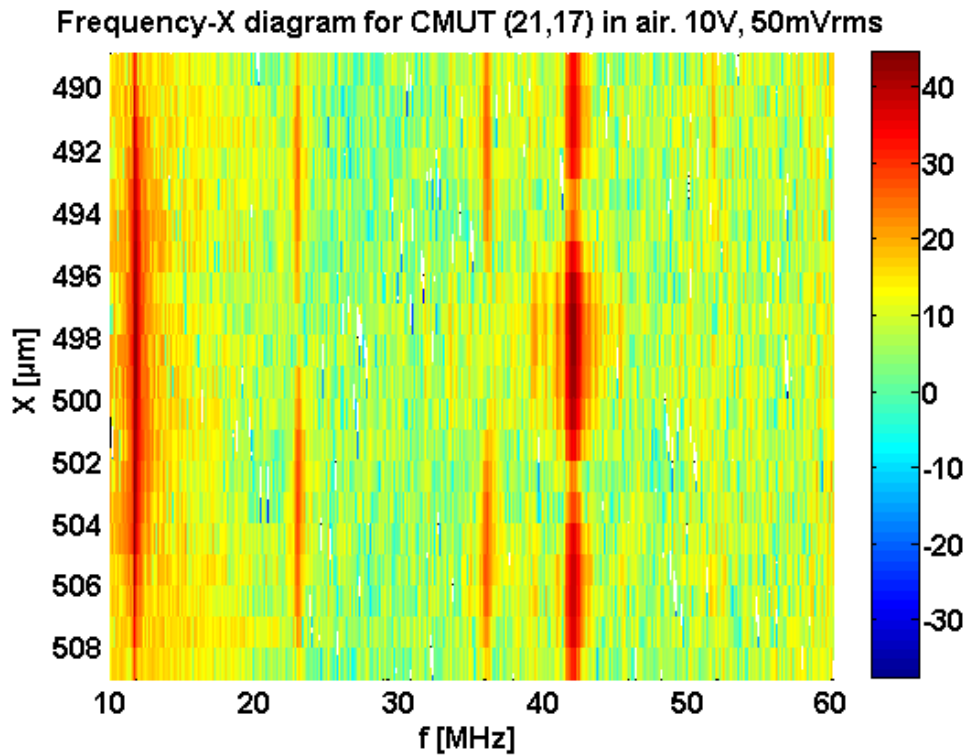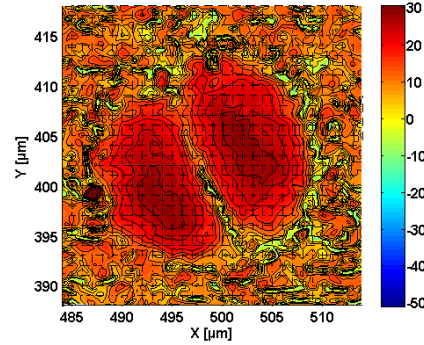
Figure 7.5: Frequency-x scan over the CMUT membrane of cell (21,17) with 10V bias
and an AC excitation of 50mV$_{\text{RMS}}$. The unit of the colour bar is decibel
picometer.

Figure 7.5 gives the impression that there are several peaks along the frequency
response. The first peak lies at 11.80MHz, which is the one that has been focused
on so far. The second peak is located at 22.97MHz. To investigate this peak
further, it was decided to perform a 2-dimensional scan of the entire CMUT cell
when excited at 22.97MHz. The result of the scan is plotted in figure 7.6. The
area between each data point has been interpolated for a better illustration.
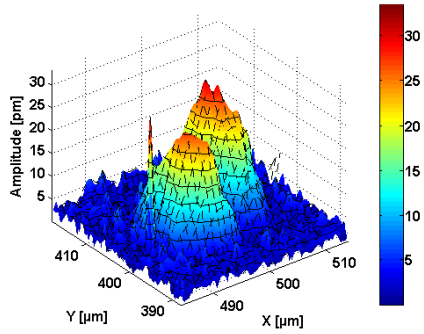
(a) Colours, contour and height represent absolute vibration amplitude. The unit of the colour bar is picometer.

(b) Colours and contour denote absolute vibration amplitude in a logarithmic scale. The unit of the colour bar is decibel picometer.
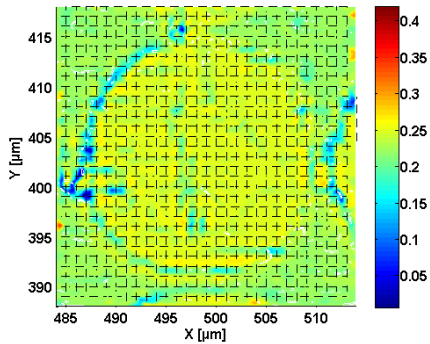
(c) Colours represent reflectivity (amplitude of I_n), and contour denotes absolute vibration amplitude. The unit of the colour bar is volt.
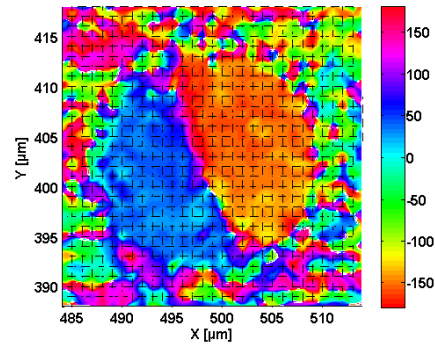

(d) Colours represent the phase of the vibrations, and contour shows absolute vibration amplitude. The unit of the colour bar is degree.

Figure 7.6: Array cell (21,17) measured at its frequency peak 22.97MHz when excited with 10V bias and 50mV$_{\text{RMS}}$

7.3   Optical measurements in oil

The planned measurements on the CMUT chip in air had at this point been completed. The next step was to immerse the sample in oil and characterize it once again. All the measurements presented here are made with a 10mm thick layer of olive oil covering the sample, unless otherwise stated. Since the membrane was covered in a fluid, more energy was required to excite vibrations. An AC voltage 10 times stronger than the one employed in air was therefore applied in the immersion measurements.

A natural first step was to determine the frequency response of some cells and compare its properties with the air measurements. Unfortunately, the cells which were tested earlier did not seem to work after the sample had been immersed. Figure 7.7 shows the result of a frequency scan made on each of two randomly chosen working cells. If we zoom in on the scan of cell (29,45) in figure 7.7, a strange ripple is observed. See figure 7.8.
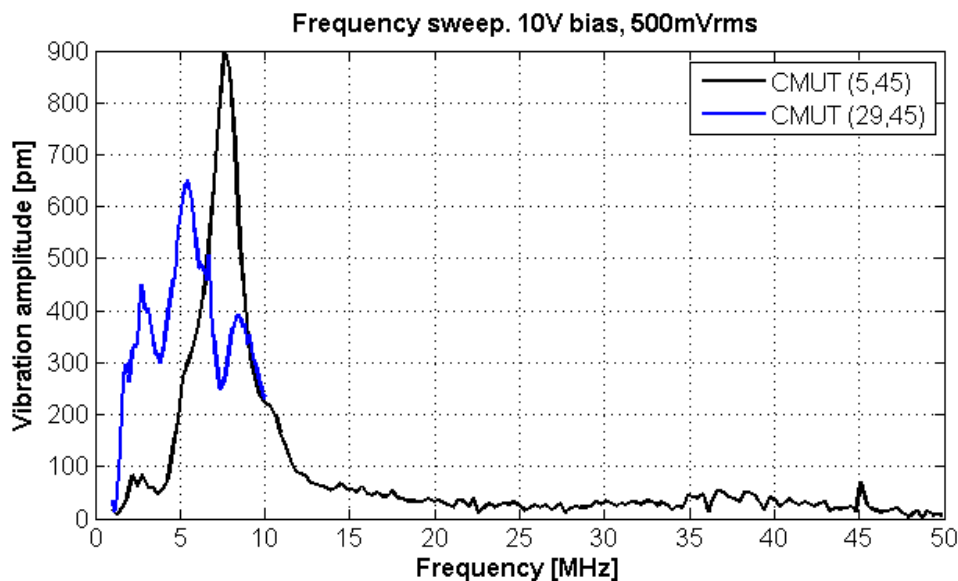

Figure 7.7: Frequency scans of array cells (5,45) and (29,45) with 10V bias and a 500mV$_{\text{RMS}}$ AC component applied.
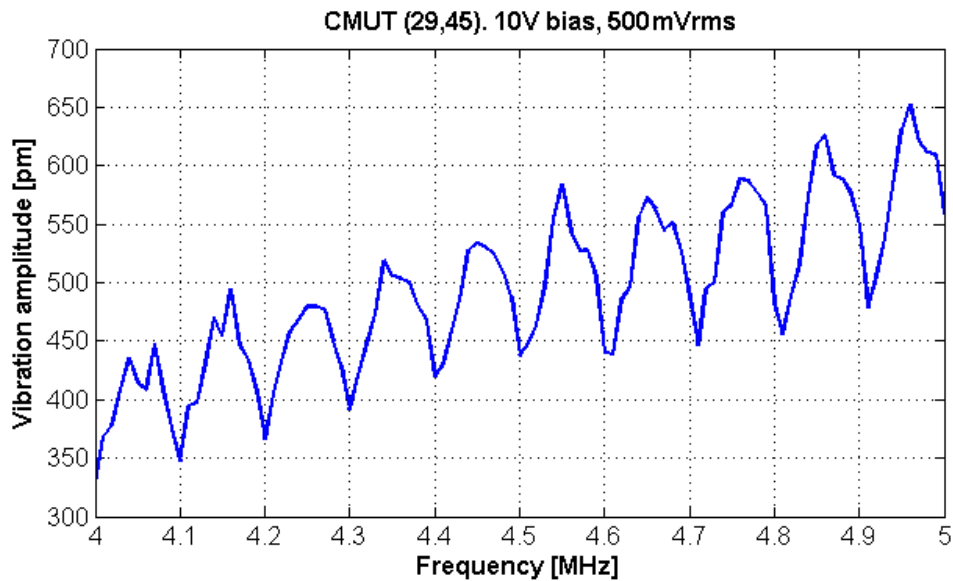
Figure 7.8: Frequency scan of array cell (29,45) with 10V bias and a 500mV$_{\text{RMS}}$ AC component applied.

The frequency response of cell (29,45) peaks at 5MHz according to figure 7.7. It was decided to perform two 2-dimensional scans at this frequency. The first scan would do a high resolution measurement of the vibration pattern of the specific cell in question. This was mostly to test the performance of the experimental setup when transmitting the probing laser through oil, but also to look for explanations behind the ripple in figure 7.8. The second 2-dimensional scan at 5MHz covered a large spatial area, one data point for every cell in the array. By performing this scan one should be able to see how the vibration pattern of an entire array would be when many cells were excited at the same time and at the same frequency. The results of the two 2-dimensional scans are depicted in figures 7.9 and 7.10.
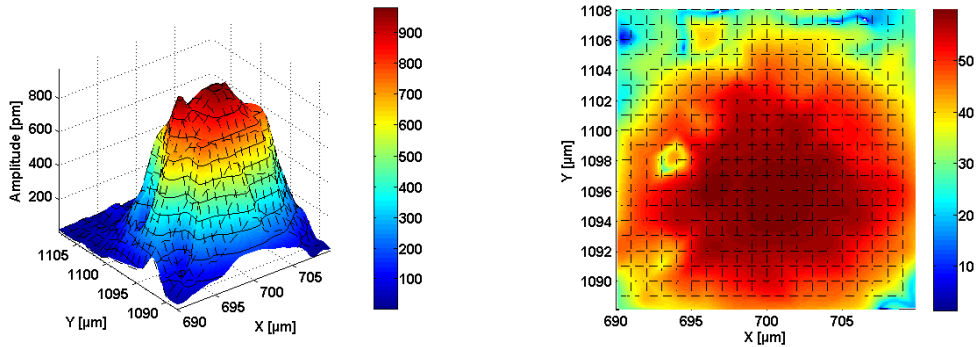
(a) Colours, contour and height represent absolute vibration amplitude. The unit of the colour bar is picometer.

(b) Colours and contour denote absolute vibration amplitude in a logarithmic scale. The unit of the colour bar is decibel picometer.
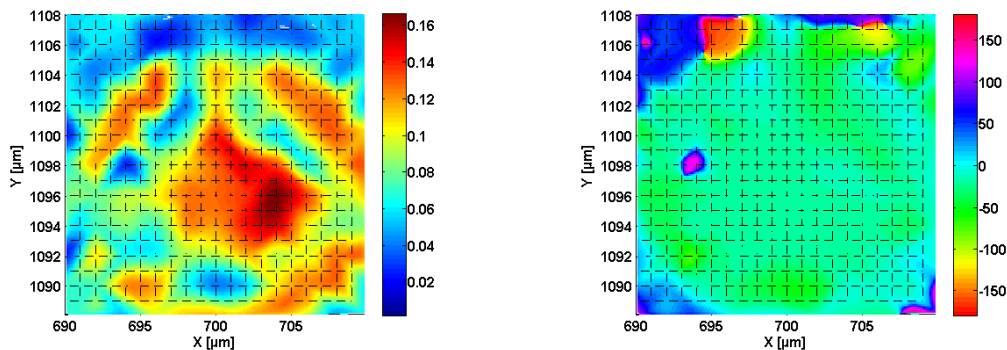
(c) Colours represent reflectivity (amplitude of I_n), and contour denotes absolute vibration amplitude. The unit of the colour bar is volt.

(d) Colours represent the phase of the vibrations, and contour shows absolute vibration amplitude. The unit of the colour bar is degree.

Figure 7.9: Array cell (29,45) measured at its resonance frequency 5MHz when excited with 10V bias and 500mV$_{\text{RMS}}$. The area between each data point has been interpolated for a better illustration.
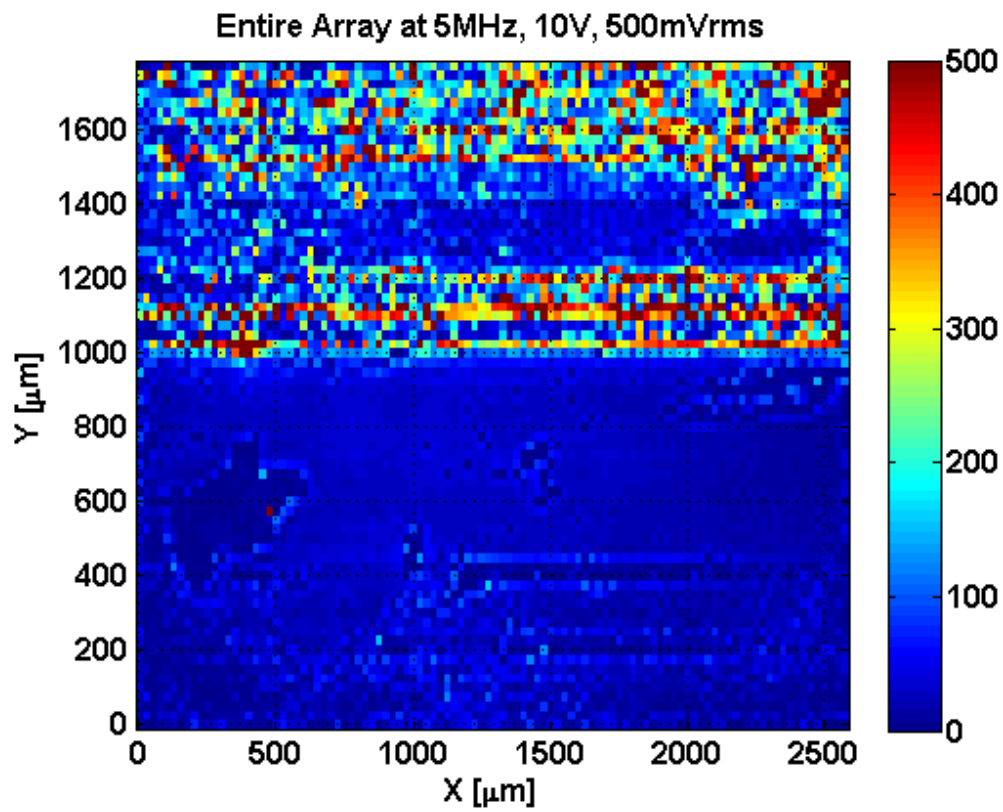
Figure 7.10: 2-dimensional scan of the entire array with 10V bias and a 500mV$_{RMS}$
AC component applied. One pixel of the colour map is equivalent to
one CMUT cell. The unit of the colour bar is picometer.

It was appropriate to conduct the same type of measurement as in figure 7.5, where a line across the membrane of a CMUT cell in air was measured at different frequencies. Comparing the scan results for the sample surrounded both by air and oil, it would be easy to visualize the effect immersion has on the frequency response. The result of the scan in oil is shown in figure 7.11.
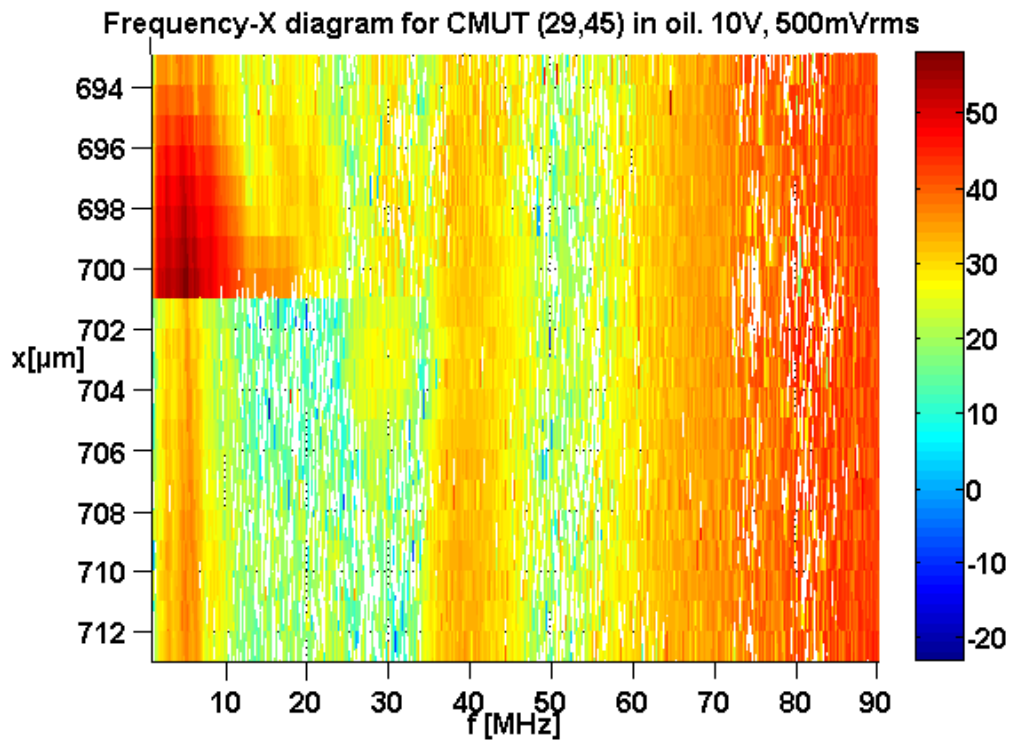
Figure 7.11: Frequency-x scan over the CMUT membrane of cell (29,45) with 10V bias and an AC excitation of 500mV$_{\text{RMS}}$. The unit of the colour bar is decibel picometer.

7.4 Electrical measurements 2

In order to prepare the next measurement, the sample was taken out of the oil and cleaned with ethanol before being connected to the ANA once again. At this point, the sample had been immersed for 5 weeks and excited by AC and DC voltage for most of this period. It was therefore decided to do a similar electrical measurement as in figure 7.2 to look for changes in the frequency response. The sample had been through a lot, and figure 7.12 shows the resulting S_{11} frequency response.
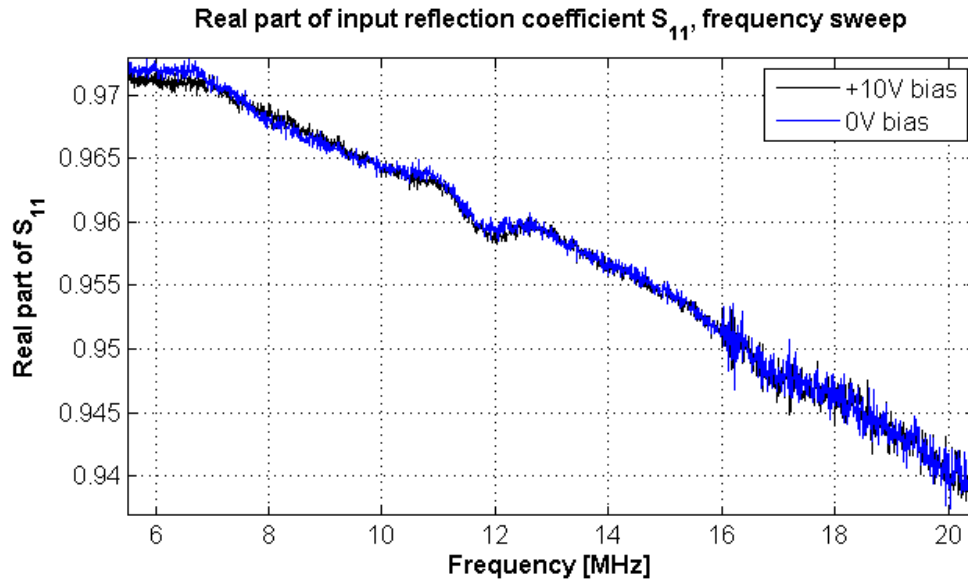
Real part of input reflection coefficient S$_{11}$, frequency sweep

(a) Real part of input reflection coefficient S_{11}

Imaginary part of input reflection coefficient S$_{11}$, frequency sweep
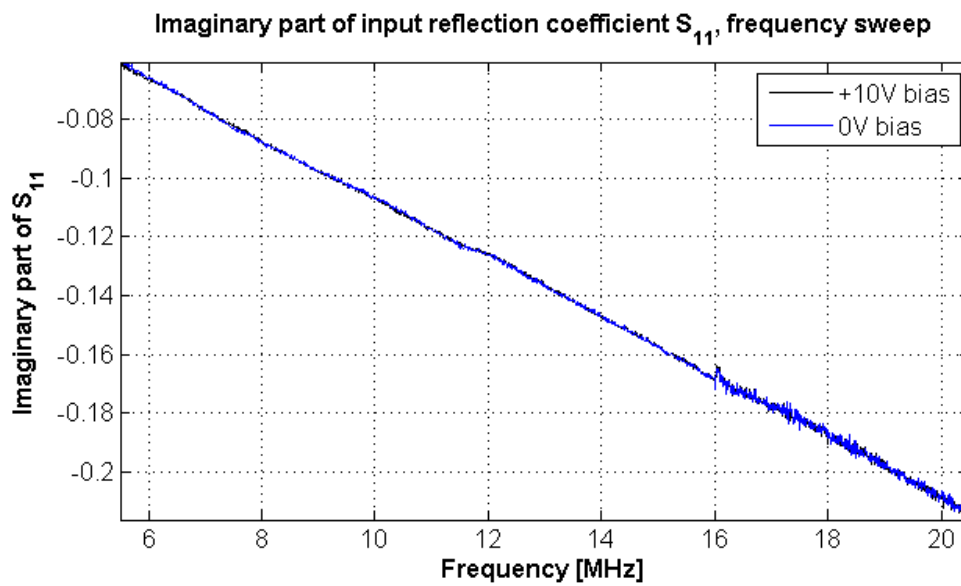
(b) Imaginary part of input reflection coefficient S_{11}

Figure 7.12: Measured input reflection coefficient S_{11} as a function of frequency. The sample was not immersed.

7.5   Discussion

7.5.1   "'Children's disease'"

The electrodes of this sample had never been subjected to any voltage before the measurement series in this chapter. But even if the sample was new, the surface features seemed to have some imperfections when examined in an optical microscope, see figure 7.1. The electrical measurements in figure 7.2 did however confirm that the CMUT was working. The ANA scans show that the resonance frequencies of the cells in air seemed to be in the area of 11MHz-14MHz.

According to the theory on CMUTs presented in section 3.1, the vibration amplitude of the membranes should be negligible when the electrodes are unbiased. The ANA measurements in figure 7.2 do suggest otherwise, though. The graph for 0V bias gave a resonance peak even larger than the graph that represents 7.2V bias. Another point which does not correlate with the theory is the fact that the 0V resonance frequency is lower than the 7.2V peak, when one actually would expect it to be the other way around. The last piece of information we can extract from the S_{11} measurements is that the CMUT array had no visible resonance frequency at 3.6V.

The questions arising from the electrical measurements are answered by the results of the first interferometric scans in figure 7.3. These scans were a set of frequency measurements focused on a single cell in the CMUT array. The applied bias was increased from 0V to 12V three times, and the frequency response was measured at four voltage increments for each scan. We notice that the scans do not fit the response from the ANA measurements perfectly. This is an interesting point, because it shows that the CMUT had an unpredictable frequency response. In the last two measurement series in figure 7.3, the unpredictable behaviour seems to have come to an end. The one thing which had changed between the first and second series is the fact that the membrane had collapsed for the first time, as the 12V measurement suggests. The collapse could have changed the mechanical properties of the CMUT. Another explanation is based on electrical charges.

Charges are known to be trapped on the membrane surface facing the cavity of the CMUT cells, as shown in ref. [30]. The extra charge difference between the electrodes would then effectively give a larger bias voltage than that applied by the generator. This can explain the results shown in figure 7.3. In the first measurement series, the 5V and 10V resonance peaks are much closer in frequency than in the last two scan series. It is more than likely that the membrane was close to collapse at 5V during the first series. During the time the voltage was increased to do the 10V scan, the membrane probably collapsed momentarily at

a certain voltage. A spark may have been triggered, releasing the surface charges under the membrane and allowing them to dissipate into the bottom electrode. At this point, the charge distribution of the membrane had probably stabilized. Thus when the DC generator reached 10V, the potential difference between the electrodes was no longer enough to collapse the membrane. These events would explain why all the 10V resonance peaks are at the same frequency. This theory also explains why the second and third measurement series were repeatable.

7.5.2 Temporal drift

Sample 1, the symmetric array, had resonance frequencies which shifted as a function of time. Since sample 2 also showed signs of charging effects, it was deemed necessary to investigate this further. Figure 7.4 shows that resonance drifting is less of a problem for this particular prototype. A leakage current from an electrode to the membrane must be present, before the charges can build up when bias voltage is applied [29]. There may have been a leakage current on sample 1, but this problem was not observed in sample 2. How the initial surface charges got to the membrane in sample 2 in the first place (see the last paragraph) is a still a mystery for the MUSIC group.

7.5.3 Multiple vibration modes

Line scans across the membrane of a CMUT for a range of excitation frequencies revealed several vibration amplitude peaks in the response. Figure 7.5 illustrates the result of this measurement. The first peak near 12MHz represents the fundamental symmetric mode of vibration, and it is this one that gives the highest acoustic power. Therefore it is this mode which is best suited for real life applications. The other red and orange parts of the plot reveal the antisymmetric modes. A 2-dimensional scan of the mode at 22.97MHz was conducted to attempt to prove that the membrane actually had an antisymmetric vibration pattern. The results are given in figure 7.6. The vibration amplitude patterns in subfigures (a) and (b) show that at a line across the CMUT cell it actually does not vibrate at all. Subfigure (c) shows the phases of the vibrations, and the different colours on the membrane indicate that two sides of it are wobbling in anti-phase with respect to each other. This measurement gives an idea about how precise the measurements of the interferometer really are.

7.5.4 Measurements in oil

Some frequency scans on the sample immersed in olive oil are given in figures 7.7 and 7.8. As expected, the bandwidths have increased, and the cells' resonance frequencies are lower than in air. The ripple in figure 7.8 actually emerges from

the acoustic waves the CMUT is generating. When the waves are reflected back from the oil surface, the CMUT membranes will receive this energy and new vibrations are formed. The result is a ripple due to constructive and destructive interference with the vibrations which are already there.

The explanation of the ripple may not be easy to understand in terms of the frequency domain. An inverse Fourier transform [15] of the ripples gives a function in the time domain which has a distinct peak at a certain point on the temporal axis. The location of the peak in the time domain equals how long it took for the acoustic wave to travel from the CMUT and back again. Knowing the velocity of sound in olive oil, one can multiply these two parameters to determine the distance the acoustic waves went before they returned to the CMUT. By adding more oil on top of the sample incrementally and doing more frequency scans it was possible to prove the theory. The measured added travelling distance of the acoustic wave was plotted as a function of millimeters of added oil and is shown in figure 7.13. Applying linear curve fitting, one can observe that the slope of the curve is $1.994 \approx 2$. The value 2 actually denotes a round trip from the sample to the surface and back again. This means that the theory is solid.
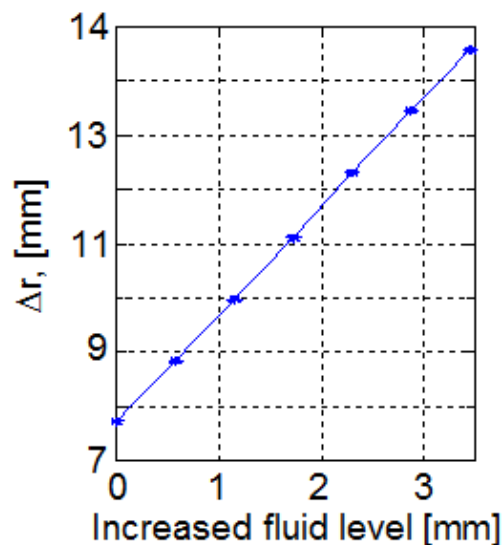
Figure 7.13: Measured change in travelling distance of the acoustic wave as a function of added oil level. The graph confirms the theory on why there were ripples in the frequency response.[5]

A 2-dimensional scan was conducted over the membrane of a cell in the array at its resonance frequency, and the figure 7.9 illustrates the result. Even if the area between each data point is interpolated, it is clear that the interferometer setup

---

[5]Particular measurement performed by PhD student Erlend Leirset, NTNU

works well, also with the sample immersed in oil. It is impossible to point out any measurement artifacts.

The second 2-dimensional scan in immersion was conducted over the whole array at 5MHz AC excitation frequency. Results are given in figure 7.10. Each spatial point of measurement was placed at the centre of the cells, so the colour of each pixel in the figure is equivalent to the maximum vibration amplitude of each cell at the given frequency. We can see that some of the rows of cells are excited, while others are not. It also seems that many cells are not functioning properly, as all the pixels representing the excited rows should be green, yellow or red to indicate a moderate or strong vibration. Many of the pixels representing cells that should be working are coloured blue in the figure, which indicates a low level of vibration. This could mean that the membranes of these cells are punctured, letting oil into the cavity and thus ruining the conditions for vibration. The light blue area where there should be no excited rows shows that there is a low level of vibration going on. These vibrations are probably induced by the ultrasonic waves emerging from the working cells after being reflected back from the oil surface. Areas where the colour of the figure is dark blue represents cells that are barely or not at all vibrating. Those cells might be damaged or have a resonance frequency far from 5MHz.

7.5.5   Durability

Figure 7.11 shows the result of the last optical measurement, which was a frequency scan across the membrane of a CMUT cell. It was discovered that the whole array stopped functioning during this scan, which explains the abrupt characteristic of the plot. After this occurrence, every electrical system and connection to the sample was checked for errors to confirm that it actually was the CMUT itself that stopped working. No errors were found in the experimental setup. The electrical measurements in figure 7.12 were done after the sample had been taken out of the oil and cleaned, and the frequency response suggests that the sample is competely dead.

What happened physically to the sample is unknown, but what we do know is that the sample had been immersed in oil for 5 weeks and heavily excited with AC voltage during that time. This could have been enough to shake it apart somehow. It must also be emphasized that the surface features on the sample seemed to have many imperfections when it was examined in a microscope. There is not sufficient evidence for stating that every CMUT of this design stops functioning after 5 weeks of immersed operation.
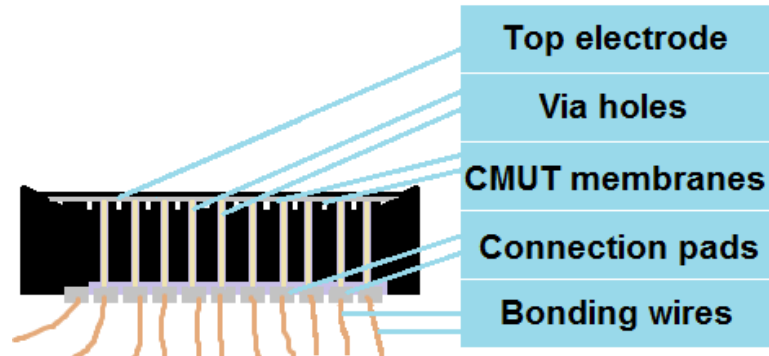
8   New circuit board suggestion

At the present time, a sample consists of one or more CMUT arrays glued to a small circuit board with conducting silver paint. The silver paint is in contact with the bottom electrode of the CMUT array and a path of paint finds its way to a copper pad on the circuit board which becomes the ground reference node. The CMUT connection pads (top electrodes) are bonded to other copper pads on the circuit board to make place for soldered connections of physically larger electrical components. Figure 8.1 illustrates how two of four CMUT elements are connected to the circuit board. The copper pads are connected to the generators via the CMUT transmit mode circuit from figure 3.2 and measurements are then ready to be made. The components of the transmit circuit are soldered to a vero board. This solution works well, but the circuit board is quite small and must be taped or glued in place to avoid spatial drift. This fact makes it impractical to move the sample from one measuring instrument to another.
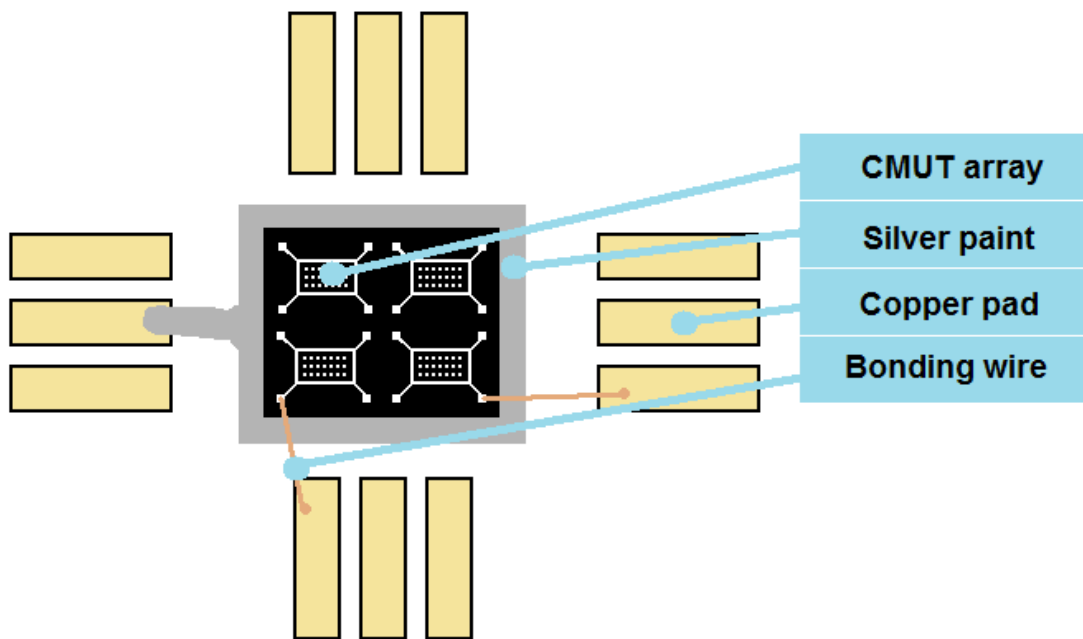
Figure 8.1: Old circuit board design: CMUTs attached by silver paint

A new CMUT prototype was produced during this thesis period, which has a somewhat different design with respect to older models. Among other changes, the CMUT connection pads are now on the opposite side of the membranes and one pad is dedicated to the substrate. That is, the top electrode connections are now made through isolated via holes which emerge on the other side of the CMUT array. The bonding wires must thus be connected on the opposite side of the membranes which should be able to be probed by laser light with the interferometer. Using the old circuit board setup would either make the membranes face

away from the laser, or crush the bonds under the weight of the sample. Figure 8.2 illustrates the problem.

Figure 8.2: New CMUT prototype: membranes and connection pads placed on opposite sides

It is clear that a new circuit board must be designed. The following suggestion will make it possible to measure the sample both with the interferometer and the network analyzer. It would be simple to unmount the sample and move it. Another new feature would be the opportunity to selectively switch on and switch off interconnected CMUT elements. On the new prototype, 4 CMUT cells make up 1 interconnected element.

The basic idea is to place the CMUT array between two plates, each plate having a layer of fibreglass under a layer of copper. One of the plates will be bonded to the CMUT pads. Copper is however a material known to be difficult to bond gold wire to. The plate should be covered with a 300nm thick layer of gold on top of a 100nm thick layer of titanium, making it a good conductor while easier to bond to. The thicknesses are known from experience. Growing the titanium and gold layers can for instance be done using electron beam physical vapour deposition.

The design of each of the two plates is shown in figure 8.3. In the plate on the left in the figure there will be drilled a square hole in the middle, slightly bigger than the size of the CMUT chip. On the same spot on the right plate, a smaller circular hole will be made. The membrane side of the CMUT chip should then be glued to the copper side of the right plate so that the membranes can "'see'" through the circular hole. Sandwiching the plates will thus reveal both sides of the CMUT, without falling through. The membranes of the CMUTs of the new prototype will be looking out of the hole of the plate that is not covered in gold and titanium. Since the optical measurements involve a laser focusing onto the membranes, the hole should be made in a cone-shape as shown in figure 8.3. This will help avoid making an unnecessary aperture for the laser when probing CMUT cells at the edges of the sample. The other holes can be drilled with less care; we will come back to them later.
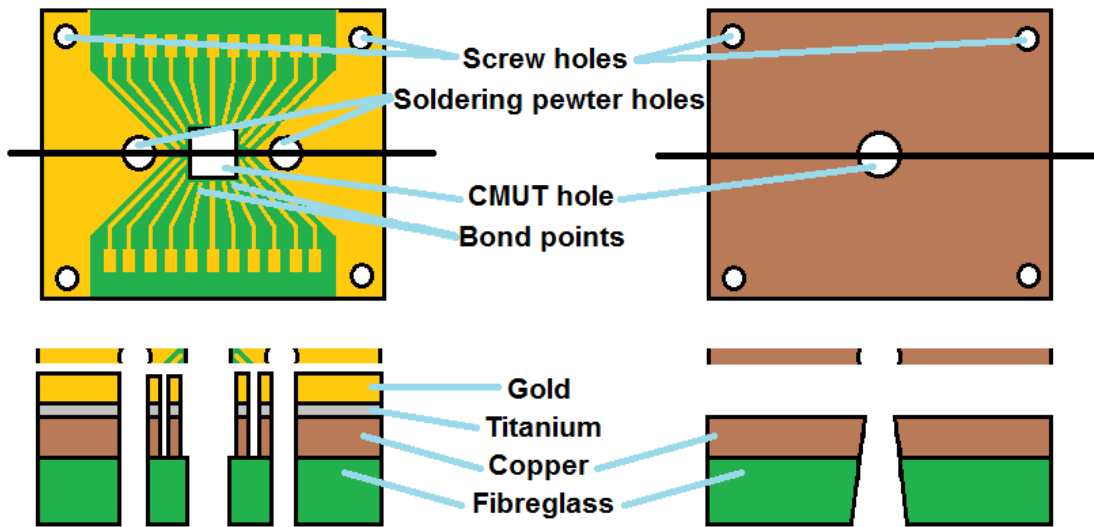
Figure 8.3: New circuit board design: the CMUT chip will be placed between these two plates. The solid black lines across the plates indicate the cross-sectional areas shown below the plates. Note that the dimensions are not to scale.

The plate on the left in figure 8.3 should be selectively milled down to the fibreglass layer to create conducting and isolating structures. 20 conducting lines must be made. 18 of these lines will later be in electrical contact with the top electrodes of the CMUT and 2 of them will be dedicated to earth i.e. the substrate.

As noted earlier, the sample should be glued in place at the hole of the fibreglass-copper plate with the membranes facing the hole. The other plate can then be fastened on top of the fibreglass-copper plate using the screw holes in figure 8.3. Filling the two soldering pewter holes shown in the figure with liquid tin will permanently bind the sample to the two plates. Both surfaces of the CMUT chip will now be positioned slightly deeper than the plates'. Gold wires can thus be tightly bonded from the CMUT connection pads to the conducting lines of the 4-layer plate without risking shorts between the electrodes of the CMUT.

Figure 8.4 will illustrate the next steps. The two merged plates with the sandwiched CMUT will now be referred to as the sample board. A flexible flat cable (FFC) connector (figure 8.5(a)) is soldered to the sample board so that each conductive line is in contact with its dedicated pin on the connector. An FFC will go into another FFC connector placed on a printed circuit board (PCB). This PCB can thus easily be connected or disconnected from the FFC connector and obviously be used several times with other sample boards.

Each line coming from the FFC connector on the PCB in figure 8.4 will be expanded into 3 lines, so that there are a total of $20 * 3 = 60$ lines entering the dual in-line package (DIP) switch. A DIP switch is a set of small manual switches which can be flipped using a pen or a small finger nail, see figure 8.5(b). As established, 3 switches now control 1 connection pad on the CMUT chip. 1 of these switches can be used to ground the CMUT pad. The 2 others each control a DC input with a protective $1M\Omega$ resistor and an AC input/output terminal with 1nF capacitors to block the DC from entering the AC terminals. 2 AC terminals are used because it gives the opportunity to use one as an input and the other as an output. This can be used to examine cross-talk effects between the CMUT elements. It is also propitious for pulse-echo measurements, using terminal AC1 to send the pulse while listening at the echo at AC2.

The circuits are designed in accordance with figures 3.2 and 3.3 in the theory section. The components should be of the surface mounted technology (SMT) type as in figure 8.5(c). This is a good idea because SMT gives increased board density and reduced weight, volume and cost [31].

A steady base could be made in addition, with screw holes fitting the ones in the sample plate. Having such a base near the different instruments used to test CMUTs would make it easy to move samples from one instrument to another and fastening it without the mess that follows with glue and tape. Being able to selectively activate transducer elements makes it much easier than before to characterize the samples in great detail. New features include characterizing different parts of the CMUT array electrically and investigating cross-talk effects just by flipping switches on the DIP component.

In order to be fair, the two inconveniences with this design must be mentioned. Number one is the fact that this solution would be more expensive than the previous one due to the many steps of production. Another problem might be that the signals of each CMUT pad may pollute each other since their conductors would be quite close in the FFC and on the PCB.

The design presented in this chapter was mainly outlined by PhD student Erlend Leirset, with the assistance of PhD student Sigrid Berg and the author.
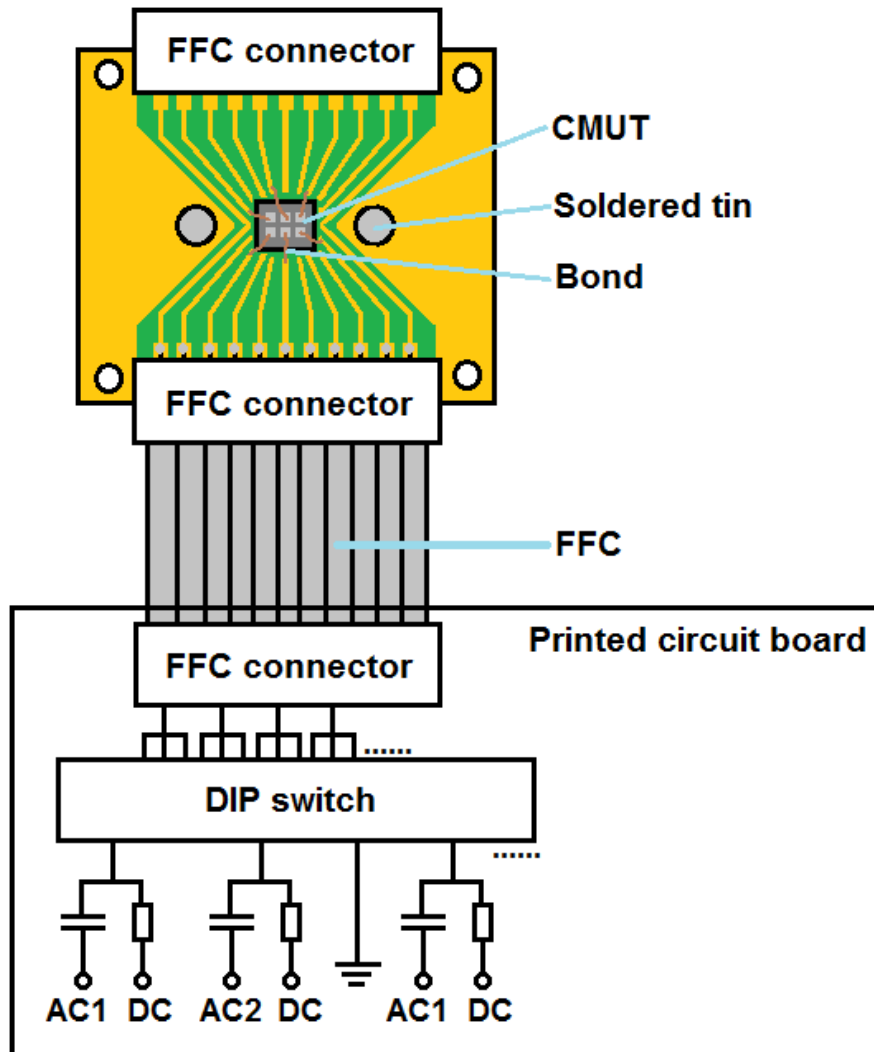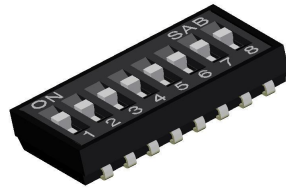
Figure 8.4: New circuit board design: the CMUT pads are bonded to the conductive
lines. Every line is elongated through an FFC to a printed circuit board.
On the circuit board, a DIP switch can selectively activate transducer
elements.
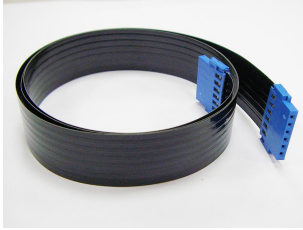
(a) Flexible flat cable

(b) Typical dual in-line package switch

(c) Surface mount resistor

Figure 8.5: Real photos of a flexible flat cable, a dual in-line package switch and a surface mount resistor[5]

---

[5]Subfigures are respectively from refs. [32], [33] and [34].

9 Conclusion

Two Capacitive Micromachined Ultrasonic Transducer (CMUT) prototypes have been characterized in this thesis. Electrical measurements with a network analyzer proved to be a fast and easy way of determining the frequency response of an interconnected transducer element comprised of several CMUT cells. Optical measurements were also performed by a heterodyne interferometer in order to probe single cells. The optical setup was extremely sensitive, being able to detect vibration phases and amplitudes down to a few picometers. Its spatial resolution is also very small, with the object beam having a radius of $\approx 0.38\mu$m at the sample plane.

The prototype tested first, referred to as sample 1, was an interconnected array of CMUTs. Network analyzer measurements showed that the frequency response had two distinct peaks at 32.2MHz and 33.3MHz near its collapse voltage in air. Two peaks so close to each other is a rare phenomenon, so the sample was tested further with the interferometer. The peaks were evidently not originating from two different vibration modes inherent in each cell. Each cell had its own unique fundamental resonance frequency, some of them close to 32.2MHz and others near 33.3MHz. It is impossible to fabricate all the cells identically, and this explains the different resonances. The resonance frequencies were also shifting as a function of how long the CMUT had been biased. Experiments showed that the drift is probably caused by charges being trapped under the membranes of the CMUTs, effectively increasing the potenial difference between the electrodes until the membranes collapse. These charging effects make the characteristics of the prototype unpredictible and should be solved before incorporating it in an ultrasonic probe.

A second prototype had resonance freqencies between 10MHz and 12MHz in air near the collapse voltage. The first measurements suggested that this sample, sample 2, was precharged. This assumption is based on the fact that the characteristics of the CMUT changed permanently after it collapsed once. Even if this is not the correct assumption, we have learned that the transducer should be collapsed at least once in order to achieve a predictible frequency response. Other charging effects were not observed. Sample 2 was also immersed in a fluid with many properties resembling blood plasma and measured optically. The bandwidth of the centre frequency became wider, and the resonances were observed near 5MHz in this case. A higher centre frequency is needed to achieve the wanted spatial resolution of the probe. The sample stopped functioning after 5 weeks of operating in immersion. This does not necessarily mean that the quality of the prototype is poor, as this particular sample seemed to have a few non-uniformities on the surface even before the measurements started.

The next prototype to be tested has different geometrical properties with respect to older models and does not fit today's experimental setups. A new way of connecting this CMUT variant to the measuring instruments is outlined in this thesis. The design is more complicated than before, but easier to handle in practice. Measuring crosstalk effects between the transducer elements would literally be as easy as flipping a switch, as the elements could selectively be switched on or off.

Future work in developing the ultrasonic probe involves characterizing more CMUT prototypes while learing about their positive and negative properties along the way. The CMUT must be improved before it is ready to be incorporated in an intravascular probe. It is still a challenge to make a reliable CMUT structure with a centre frequency of $30 - 50\text{MHz}$ in blood. When this challenge is overcome, the next steps involve designing the electronics and figuring out how the CMUTs should be distributed on the probe.

References

[1] P. Libby, "Inflammation in atherosclerosis," *Nature*, vol. 420, 2002.

[2] A. S. Ergun, G. G. Yaraliogly, and B. T. Khuri-Yakub, "Capacitive micromachined ultrasonic transducers: Theory and technology," *Journal of aerospace engineering, Vol 16, No. 2*, 1-apr-2003.

[3] E. Jeanne, C. Meynier, J. Terry, M. Roy, L. Haworth, and D. Alquier, "Evaluation of parylene as protection layer for capacitive micromachined ultrasonic transducers," *ECS Transactions, 11 (16) 25-33*, 2008.

[4] S. H. Wong, M. Kupnik, R. D. Watkins, K. Butts-Pauly, and B. T. Khuri-Yakub, "Capacitive micromachined ultrasonic transducers for therapeutic ultrasound applications," *IEEE Transactions on Biomedical Engineering*, 2009.

[5] M. I. Haller and B. T. Khuri-Yakub, "1-3 composites for ultrasonic air transducers," *IEEE Ultrasonics Symposium*, 1992.

[6] F. Teston, C. Meynier, E. Jeanne, N. Felix, and D. Certon, "Characterization of standard cmut devices based on electrical impedance measurements," *Ultrasonics Symposium, IEEE*, oct-2006.

[7] H. Martinussen, A. Aksnes, and H. E. Engan, "Wide frequency range measurements of absolute phase and amplitude of vibrations in micro- and nanostructures by optical interferometry," *Opt. Express*, vol. 15, no. 18, pp. 11370–11384, 2007.

[8] K. Midtbø, A. Rønnekleiv, and D. T. Wang, "Fabrication and characterization of cmuts realized by wafer bonding," *Ultrasonics Symposium, 2006. IEEE*, pp. 938–941, 2-6 Oct. 2006.

[9] K. Midtbø, K. Schølberg-Henriksen, M. M. V. Taklo, and A. Rønnekleiv, "Surface energy of fusion bonded silicon nitride to silicon," *The Eight International Symposium on Semiconductor Wafer Bonding, Quebec City, Canada*, 2005.

[10] G. Caliano, R. Carotenuto, E. Cianci, V. Foglietti, A. Caronti, A. Lula, and M. Pappalardo, "Design, fabrication and characterization of a capacitive micromachined ultrasonic probe for medical imaging," *IEEE Transactions on Ultrasonics Ferroelectrics and Frequency Control, vol. 52, pp. 2259-2269*, 2005.

[11] R. Foy and F.-C. Foy, *Optics in astrophysics.* Springer Science + Business Media, Inc., 2005.

[12] P. Hariharan, *Optical Interferometry*. Academic Press, second ed., 2003.

[13] P. M. Mather, *Computer processing of remotely sensed images: an introduction*. John Wiley & Sons, Inc., third ed., 2004.

[14] B. E. A. Saleh and M. C. Teich, *Fundamentals of Photonics*. John Wiley & Sons, Inc., second ed., 2007.

[15] K. Rottmann, *Matematisk formelsamling*. Spektrum Forlag, 2003.

[16] E. Leirset, "Heterodyne interferometry," *Norwegian University of Science and Technology*, 2008.

[17] A. Korpel, *Acousto-optics*. CRC Press, second ed., 1996.

[18] "`http://www.rp-photonics.com/acousto_optic_modulators.html`," 03-nov-2009.

[19] D. M. Pozar, *Microwave and RF design of wireless systems*. John Wiley & Sons, Inc., 2001.

[20] Agilent Technologies, Inc., *Network Analyzer Basics*, 2004.

[21] D. B. J. et al., *Acoustic wave sensors : theory, design, and physico-chemical applications*. San Diego: Academic Press, 1997.

[22] H. Kogelnik and T. Li, "Laser beams and resonators," *Applied optics, Vol 5, No. 10*, 1966.

[23] W. Menke, *Geophysical data analysis: discrete inverse theory*. Academic Press, Inc., second ed., 1989.

[24] J. Y. Lee, B. H. Wong, W. Y. Kim, S. K. Min, Y. Kim, M. V. Jouralev, R. Bose, K. S. Kim, I. Hwang, L. J. Kaufman, C. W. Wong, P. Kim, and K. S. Kim, "Near-field focusing and magnification through self-assembled nanoscale spherical lenses," *Nature*, vol. 460, 2009.

[25] SMIDA - oppsummering av resultater, *Note by Arne Rønnekleiv, NTNU*, 2010.

[26] Agilent Technologies, Inc., *S-Parameter Design: Agilent AN 154 Application note*, 2006.

[27] H. Martinussen, A. Aksnes, and H. E. Engan, "Investigation of charge diffusion in cmuts using optical interferometry," *Ultrasonics Symposium, IEEE*, 2008.

[28] H. Amjadi, "Charge storage in double layers of silicon dioxide and silicon nitride," *Proceedings of the 9th International Symposium on Electrets*, 1996.

[29] Y. Huang, E. O. Hæggström, X. Zhuang, A. S. Ergun, and B. T. Khuri-Yakub, "A solution to the charging problems in capacitive micromachined ultrasonic transducers," *IEEE transactions on ultrasonics, ferroelectrics and frequency control*, vol. 52, 2005.

[30] K. Midtbø and A. Rønnekleiv, "Analysis of charge effects in high frequency cmuts," *IEEE Ultrasonics Symposium*, 2008.

[31] Intel corporation, *Intel Packaging Databook*, 2000.

[32] "`http://www.prodata.com.tw/product-data,signal-cables.htm`," 27-may-2010.

[33] "`http://www.diytrade.com/china/4/products/4799182/DIP_SWITCH_ROTARY_SWICH_TACK_SWITCH.html`," 27-may-2010.

[34] "`http://members.cox.net/codesuidae/DCMod.html`," 27-may-2010.

A Acousto-optic modulator datasheet

1250C

Acousto-Optic Modulator

ISOMET
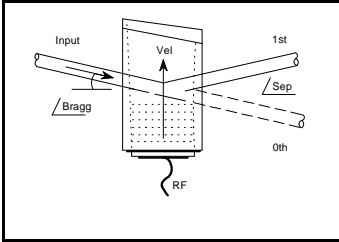
APPLICATION

- Wideband Modulator
- Frequency Shifter

FEATURES

- Very High Video Bandwidth
- Low Drive Power
- Compact
- Good Temperature Stability

DRIVERS

525C-L (DIGITAL MODULATION)   **620C-200 (VARIABLE FREQUENCY & DIGITAL MOD'N)**
535C-L (ANALOG MODULATION)   **630C-200 (VARIABLE FREQUENCY & ANALOG MOD'N)**

OUTLINE DRAWING
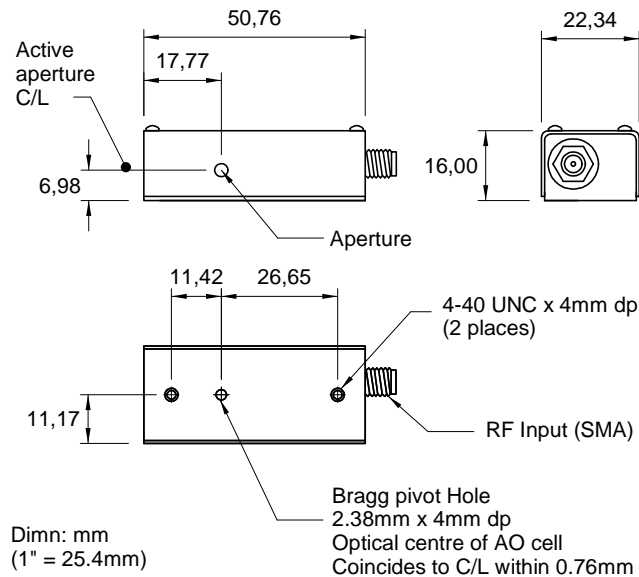
[*Please refer to 1205/06/50C-NIR Data sheet addendum for performance at wavelengths > 800nm]

1250C

Acousto-Optic Modulator

ISOMET

1106
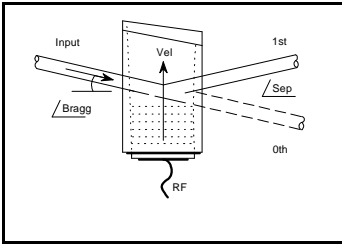
SPECIFICATIONS

Spectral Range:	.442-> 1.5μm*
Standard A/R Wavelengths:	442-488nm, 488-633nm (Options to 1.5um available)
Interaction Medium:	Lead Molybdate (PbMo0$_4$)
Acoustic Velocity:	3.63mm/μs
Active Aperture:	0.75mm
Centre Frequency:	200MHz
RF Bandwidth:	100MHz
RF Input Impedance:	50Ω Nominal
DC Contrast Ratio:	>1000:1 min (2000:1 typical)

PERFORMANCE vs. BEAM DIA. at 515nm
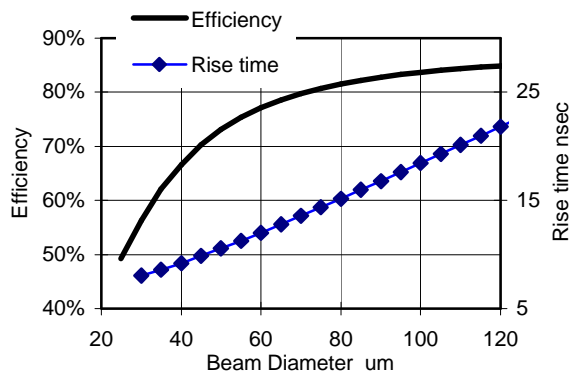
PERFORMANCE vs. WAVELENGTH

Operating Wavelength (nm)	442	488	515	633
RF Drive Power (W):	<0.7	<0.8	<0.9	<1.3
Input Bragg Angle (mrad):	12.1	13.4	14.2	17.4
0th-1st Order Beam Separation (mrad):	24.3	26.9	28.4	34.9
Static Insertion Loss (%):	<10	<5	<3	<3

MTF
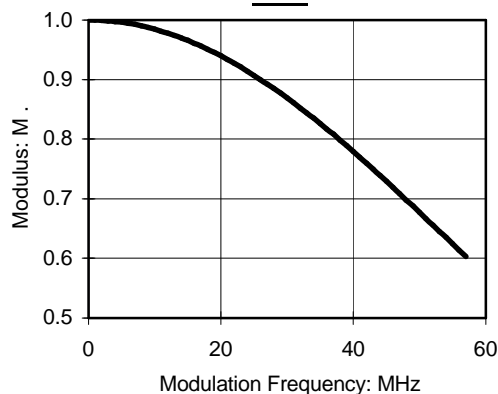
DYNAMIC CONTRAST RATIO

Maximum modulation bandwidth (50MHz) dynamic contrast ratio (CR) is obtained with a focussed beam diameter of 31μm. The typical MTF (depth of modulation) curve for the 1250C is shown at left. For larger beam diameters, the abscissa scales linearly. The value of M from the curve may be used to determine the sine wave contrast ratio at a particular modulating frequency according to the relation:

$$CR = 1+M/1-M$$

For digital, on-off modulation, the CR will be greater than the value calculated from the above equation.

B   Avalanche photo diode datasheet

APD module
C5658

Detects optical signals at 1 GHz, with high sensitivity

APD module C5658 is a highly sensitive photodetector consisting of a Si APD (avalanche photodiode), a bias power supply and a low-noise amplifier, all integrated into a compact case. The APD used has an effective active area of ϕ0.5 mm to allow efficient coupling to a light beam in applications such as spatial light transmission. The APD internally multiplies the photocurrent to produce an ample gain (set to 100 times for C5658) and also features high-speed response, achieving detection limits up to 1 GHz wideband and -48 dBm (16 nWr.m.s.) noise level in combination with the low-noise amplifier. C5658 also incorporates a thermosensor and a temperature-compensated bias power supply necessary for stable operation of the APD. Highly sensitive optical measurements can be made just by supplying +12 V to C5658.

Features

- High-speed response and high sensitivity
- Flat frequency characteristics
- Compact and lightweight
- Single power supply operation

Applications

- Laser radar
- Spatial light transmission
- Optical rangefinder

■ Absolute maximum ratings

Parameter	Condition	Value	Unit
Supply voltage		+13.5	V
Maximum incident light level	Continuous input	10	mW
Operating temperature		0 to +50	°C
Storage temperature		-20 to +70	°C

■ Electrical and optical characteristics (Ta=25 °C, Vcc=12 V, output terminated with 50 Ω)

Parameter	Condition	Typ.	Unit
Spectral response range		400 to 1000	nm
Active area		ϕ0.5	mm
Quantum efficiency	λ=800 nm	70	%
Cut-off frequency (-3 dB)	High band	1	GHz
	Low band	50	kHz
Detection sensitivity	λ=800 nm	2.5×10^5	V/W
Gain stability	25 °C ± 10 °C	±5.0	%
Noise level	Dark state	-48	dBm
Output impedance		50	Ω
VSWR *		1.5	-
Compression point at 1 dB		3	µW

* VSWR (Voltage Standing Wave Ratio)
If internal matching of elements on a signal transmission line (matching between element input/output impedance and signal line impedance) is poor, signal reflections occur that generate standing waves on the signal line. The VSWR is the ratio of standing wave maximum amplitude (V Max.) to minimum amplitude (V Min.) and indicates how well the impedance is internally matched. When this internal matching is complete, no standing waves exit and the VSWR is 0 (zero).
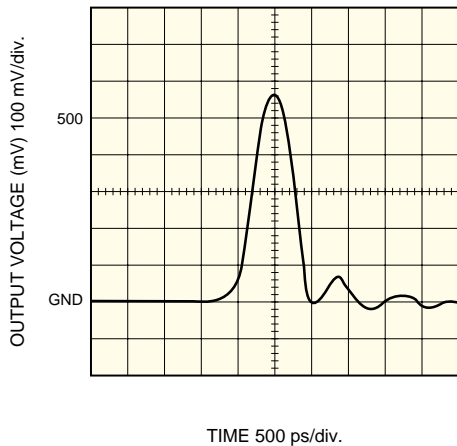
■ Signal connector

Parameter	Standard
Signal output	SMA
Power supply connector	D-sub 9 pin

■ General specifications

Parameter	Condition	Value	Unit
Supply voltage		+12 ± 0.1	V
Current consumption		100	mA
Dimensional outline	Excluding projecting parts	28 × 50 × 60	mm
Weight		120	g

SOLID STATE DIVISION

HAMAMATSU

■ Pulse response waveform

TIME 500 ps/div.

KACCB0050EA

■ Frequency response

FREQUENCY
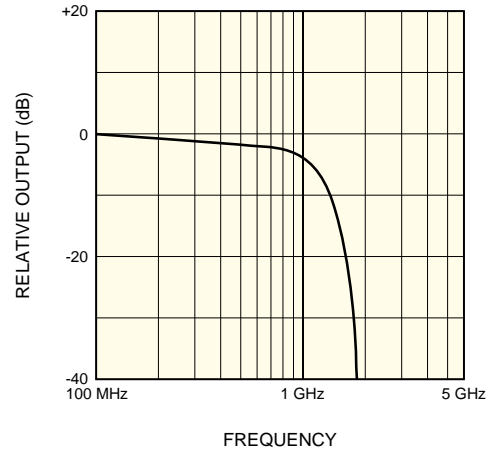
KACCB0051EB

■ Block diagram

GAIN : -100
CUT-OFF FREQUENCY (HIGH BAND: 1 GHz / LOW BAND : 50 kHz)

SIGNAL OUTPUT

50 Ω

THERMOSENSOR

APD

TEMPERATURE-COMPENSATED BIAS VOLTAGE -200 V
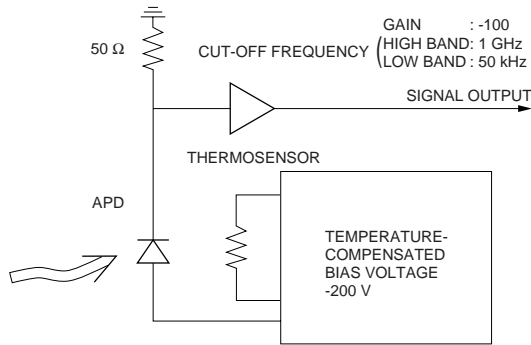
KACCC0135EB

■ Dimensional outline (unit: mm)

ACTIVE AREA

PHOTOSENSITIVE SURFACE

SIGNAL OUTPUT CONNECTOR (SMA)

1.0

60.0
50.0

28.0

4.5

50.0

POWER SUPPLY CONNECTOR (D-SUB)

MOUNTING THREADED HOLE M6 (DEPTH: 6)
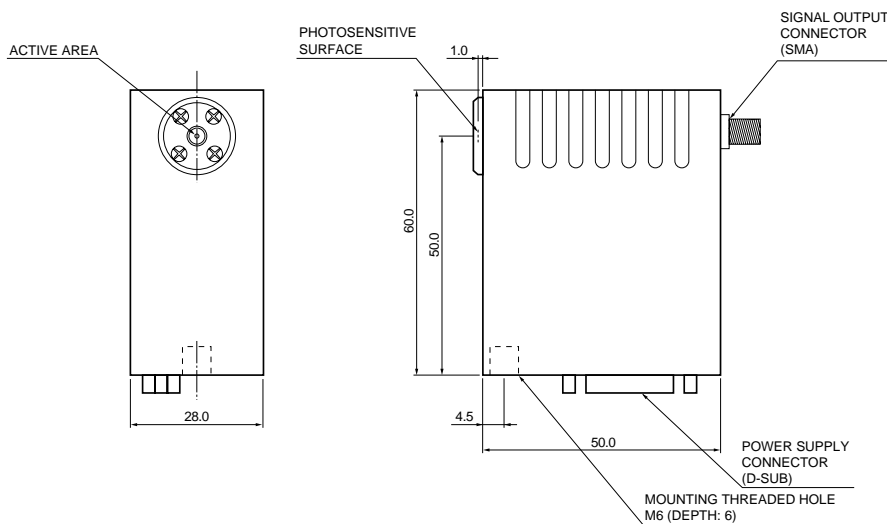
KACCA0092EA

■ Pin connection
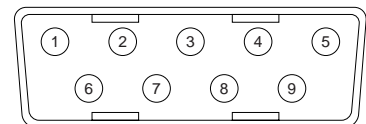
KACCC0134EA

Pin No.	Signal
1	+12 V
2	NC
3	GND
4	NC
5	NC
6	NC
7	NC
8	NC
9	NC

Mating connector (supplied):

DE-9S (made by JAE) or equivalent

2